Research Article

The Aerodynamic Characteristics of a Diamond Joined-Wing Morphing Aircraft

Shuai Miao [iD],[1] **Xiaoyong Ma** [iD],[1] **Cheng Chen**,[2] **Binhua He**,[1] **and Yong Huang**[1]

[1]*High Speed Aerodynamics Institute, China Aerodynamics Research and Development Center, Mianyang, Sichuan 621000, China*
[2]*Aerospace Technology Institute, China Aerodynamics Research and Development Center, Mianyang, Sichuan 621000, China*

Correspondence should be addressed to Xiaoyong Ma; maxiaoyong@cardc.cn

This paper presents a new-concept aircraft with a diamond joined-wing morphing configuration, which simultaneously adjusts the sweep angles of both the front wing and rear wings by a telescopic support rod. The compressible Navier-Stokes equations in the conservative form are solved to analyze the configuration characteristics and the aerodynamic benefits of this aircraft with different values of sweep angle ($15°$, $60°$) and Mach number. The maximum lift-to-drag ratio is about 13.5 at $M = 0.5$ and $\alpha = 4°$, 12.8 at $M = 0.75$ and $\alpha = 4°$, and 3.4 at $M = 1.5$ and $\alpha = 6°$, respectively. Compared with traditional morphing aircraft, the main advantages of this configuration include better transonic and supersonic performance, better lift characteristics in the state of a high-aspect ratio, and lower zero-lift drag in the supersonic state. The lift ratio of the front and rear wings shows a good similarity at different Mach numbers, especially for the $15°$ model, and the value eventually tends to be 1.3 at $\alpha = 12°$. Meanwhile, the flow field characteristics and interference characteristics of the front and rear wings are studied. The increase in the angle of attack, incoming flow velocity, and distance between the front and rear wings can reduce the interference between front and rear wings. The influence from upstream components is proven to improve the aerodynamic characteristics of the rear wing, especially at $\alpha = 8°$.

1. Introduction

Morphing aircraft is one of the most important development directions of advanced aircraft in the future and is at the forefront of innovative research in the aerospace area. In military application, its good performance is mainly reflected in the cross-speed domain, cross-media, and other aspects. As for the transonic intelligent morphing combat aircraft, the advantages are focused on short take-off and landing distances, good acceleration performance, and supersonic flight capabilities. Further, it is also featured by economic cruise, surveillance, rapid arrival, and penetration in modern warfare [1]. Wlezien et al. defined the objectives of morphing aircraft as efficient flight and multipoint adaptability to macro- and microenvironments [2], implying that morphing is the bridge between flight mission and flight performance. Thus, it is necessary to investigate further the morphing aircraft's

configuration and morphing mode to better balance adaptability to environments and flight performance.

Most studies related to morphing aircraft have focused on the morphing of wings [3–5], as the wing is the primary source of lift and handling force. Of course, there is also a great part of research dealing with the morphing of wing control surfaces like ailerons and flaps [6–8]. In recent years, with the rapid developments of technologies such as adaptive technology, intelligent materials, miniature high-energy actuators, and flexible skins, many studies have been conducted on the variable swept wing. Terrence [9] had expounded on the advantages of the swept-forward wing and swept-back wing as well as the developments and challenges of morphing aircraft. The main reasons for the development of variable-sweep aircraft are the new demands of function and performance for aircraft in the military: (1) long-range subsonic cruise combined with long endurance on the station, (2) high subsonic speed interception

combined with low-altitude transonic strike, and (3) operation from limited length runways (such as aircraft carriers) combined with requirements of high speed and maneuverability. Different swept wing angles will bring noticeable differences in aerodynamic characteristics for aircraft in various flight environments. Lv and Lv et al. [10, 11] explained property rules of variable swept wings in different heights for a BWB aircraft. According to this study, the optimal sweep angle is 20° at $M = 0.4 \sim 0.5$, which is unrelated to altitude. The optimal sweep angle changes with height at $M = 1.0$, and it is greater than 50° at different heights. In addition to the application in conventional aircraft, the variable swept wing also allows hypersonic aircraft's wide speed range and large flight envelope. Numerical and experimental investigations of a variable swept wing for an unmanned aerial vehicle at $M = 0.8/1.5/3/8$ by Tarabi et al. [12] point that the variable swept wing brings low benefits to the aircraft in the hypersonic phase, but in the transonic and low supersonic phase, the maximum lift-to-drag ratio of the aircraft has increased by about 80%.

From the perspective of the two-dimensional airfoil, the relative thickness of the airfoil changes with the sweep angle. Su et al. [13] studied the variable forward-swept wing aircraft: the lift coefficient and moment coefficient are negatively correlated with the relative thickness and the drag coefficient is positively correlated with the relative thickness. From the perspective of the aircraft, the change of the sweep angle will make the configuration significantly change. To better improve the aircraft's flight performance in different flight environments, it is necessary to use the characteristics of swept forward wing, straight wing, and swept-back wing. Li et al. [14] studied the influence of the area of the forward-swept wing, the forward-sweep angle of the quarter-chord line of the forward-swept wing, the relative thickness of the forward-swept wing's airfoil, and the position of the forward-swept wing relative to the main wing on the transonic aerodynamic characteristics of the whole aircraft. Liu et al. [15, 16] investigated a new configuration technology: the combination of canard tailless configuration, wing-body configuration, and variable swept forward wing, which enables the aircraft to have good take-off and landing capability in the subsonic state, good stall characteristics at the high angle of attack in the transonic state, and low drag and high stealth characteristics in the supersonic state. With the increasing sweep angle, the movement direction of the aerodynamic center is opposite to the change direction of the forward-swept wing, the same as the change direction of the backward swept wing. So the variable swept forward wing configuration has less problem with excessive static margins than the variable swept backward configuration. The investigation by Brett and Robert [17] shows that a 47% reduction in the maximum static margin was found to occur for a variable swept forward wing configuration relative to a similar variable swept backward wing. Nevertheless, the swept forward wing has problems of roll control and aeroelasticity; the backswept wing faces the difficulty of operating surface failure caused by airflow separation.

The studies of morphing aircraft mainly focus on traditional configuration, such as flying wing configuration and delta wing configuration. There is less research on the morphing application of diamond joined-wing configuration. The joined-wing configuration was first proposed by Wolkovitch [18] in the 1970s. Its initial design connected the front wing and the tail by the rear wing. There are also some references, which noted it as the box wing. The configuration of the front wing with the sweepback angle and the rear wing with the forward-swept angle gives the aircraft significant advantages in many aspects: (1) the wingtips of the front wing and rear wing are connected, which form a frame structure and can effectively increase the structural rigidity of the aircraft and reduce the structure weight [19–21]. A reduction of the induced drag in subsonic flight can be added among the benefits of closed or box wings, due to their effect of the reduction of the wingtip vortex intensity. (2) Compared with other conventional configuration aircrafts, under the condition of the same lift, the span length of the diamond joined wing can be reduced by 20%-30%. Meanwhile, the characteristics of the swept forward wing and swept back wing can reduce the wave drag at high subsonic speeds. The diamond joined wing also has good stall characteristics at a high angle of attack [22, 23]. (3) The diamond joined-wing wing configuration has four wings, so the reasonable arrangement of control surfaces can significantly improve the control ability of the aircraft [22, 24]. Typically, the distance between the control surfaces of the wing and the focus is large, and it will bring excellent longitudinal control characteristics to the aircraft. (4) Some tests show that the rear wing can not only provide the extra lift but also bear the bending moment of the front wing or increase the aspect ratio of the front wing and reduce the induced drag under the same wingspan and weight [24]. Djojodihardjo [25] conducted a conceptual design of a diamond joined-wing jet aircraft. Compared with the conventional configuration aircraft, it can reduce the structural weight by 5%, provide 1.35 times the lift, and reduce the drag by 3.5%. Chau and Zingg [26] designed a Mach-0.78 strut-braced-wing regional jet. Compared to the E190-E2, the strut-braced-wing regional jet offers a 12.9% improvement in the cruise lift-to-drag ratio, which means a 7.6% reduction in block flue for the nominal mission. Rasmussen [27] judged from the existing references that the current research of the diamond joined-wing configuration mainly focuses on a fixed wing. The military applications are mostly about the high-altitude long-endurance cruise for detection, and the flight speed range is subsonic and transonic [28].

The research object of this work is a new-concept aircraft with a diamond joined-wing morphing configuration and large-scale deformation. Due to the limitations of configuration and structure, the range of the aircraft's sweep angle is 15°~60°. On the premise of inheriting and expanding the advantages of morphing, it also abates the disadvantages of the configuration and the relevant morphing modes mentioned above to a certain extent. This configuration is investigated herein using both numerical simulation and wind tunnel test in terms of aerodynamic characteristics at

(a) .15° model

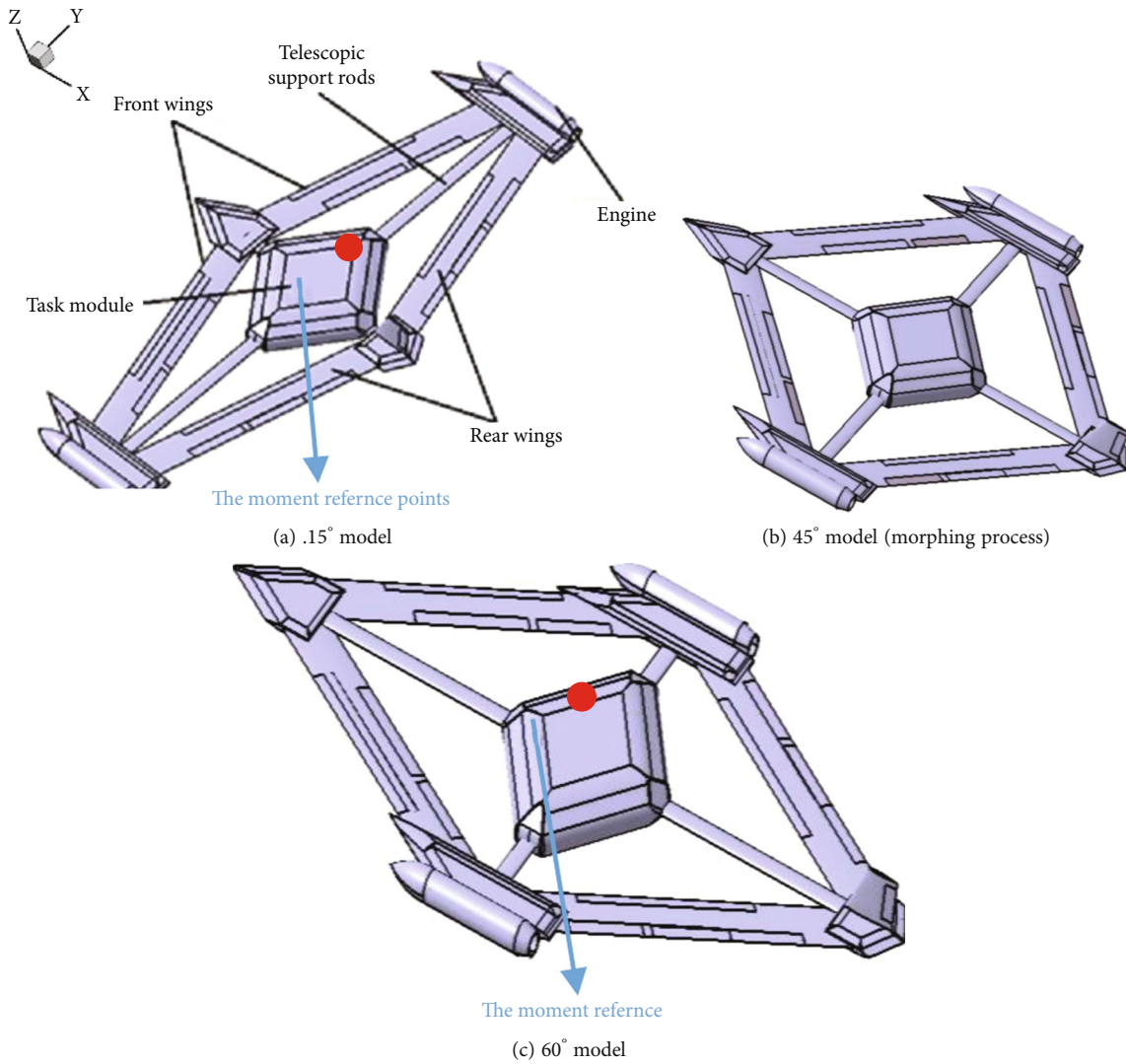(b) 45° model (morphing process)

(c) 60° model

FIGURE 1: The diamond joined-wing morphing configuration.

subsonic, transonic, and supersonic states. The flow mechanism at the typical conditions is also accessed.

2. The Diamond Joined-Wing Morphing Aircraft

The research object of this work is a new-concept aircraft with a diamond joined-wing morphing configuration. Figure 1(a) illustrates its main components: two front wings, two rear wings, a task module, and two engines. Under different flight speeds and flight states, the length of the telescopic support rod can be adjusted to change the sweep angles of the front wings and rear wings, achieving good aerodynamic performance. Meanwhile, the tilting angles of the two engines, which are independent of each other, can also be adjusted to allow the aircraft to take off and land vertically. Natural laminar flow airfoils with low resistance are used for both front and rear wings. Additionally, in terms of functionality, the requirements of various missions

can be realized by replacing the equipment in the task module.

The geometric parameters of the entire aircraft will change with the sweep angle. Table 1 shows the geometric parameters before and after the reduction of the two sweep angle state models. We position the aircraft cabin's

TABLE 1: Geometric parameters of models.

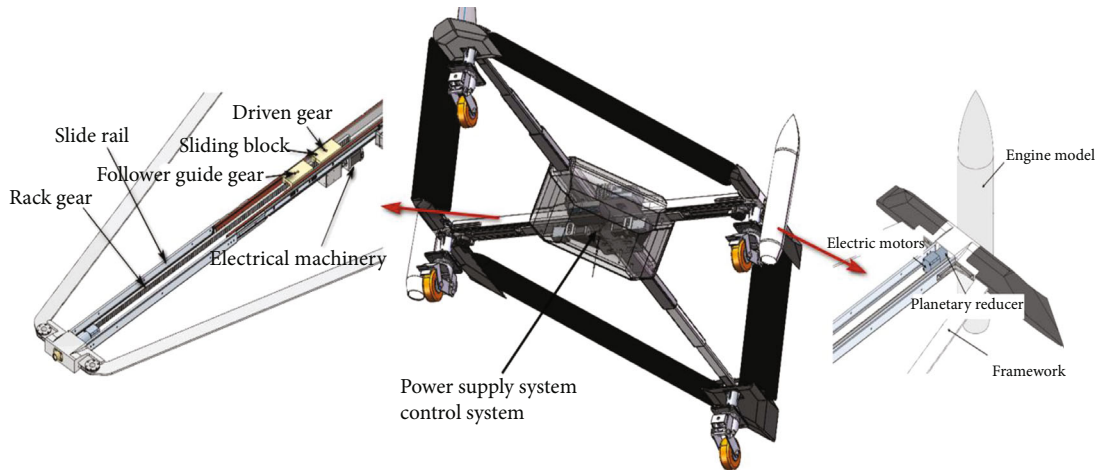| Scaling	(1 : 1)		(11.47 : 1)	
Sweep angle	15°	60°	15°	60°
Wing chord	0.6000 m	1.1580 m	0.0523 m	0.1009 m
Wing length	4.6317 m	4.6317 m	0.4039 m	0.4039 m
Wing area	2.7790 m²	2.7790 m²	0.0211 m²	0.0211 m²
Four wings area	11.1161 m²	11.1161 m²	0.0845 m²	0.0845 m²
Model length	4.8558 m	10.1093 m	0.4235 m	0.8816 m
Model span	10.3200 m	5.6835 m	0.9000 m	0.4957 m
Model high	0.9399 m	0.9399 m	0.0819 m	0.0819 m

Figure 2: The morphing verification vehicle.

(a) The 15° model of the wind tunnel test

(b) The 60° model of the wind tunnel test
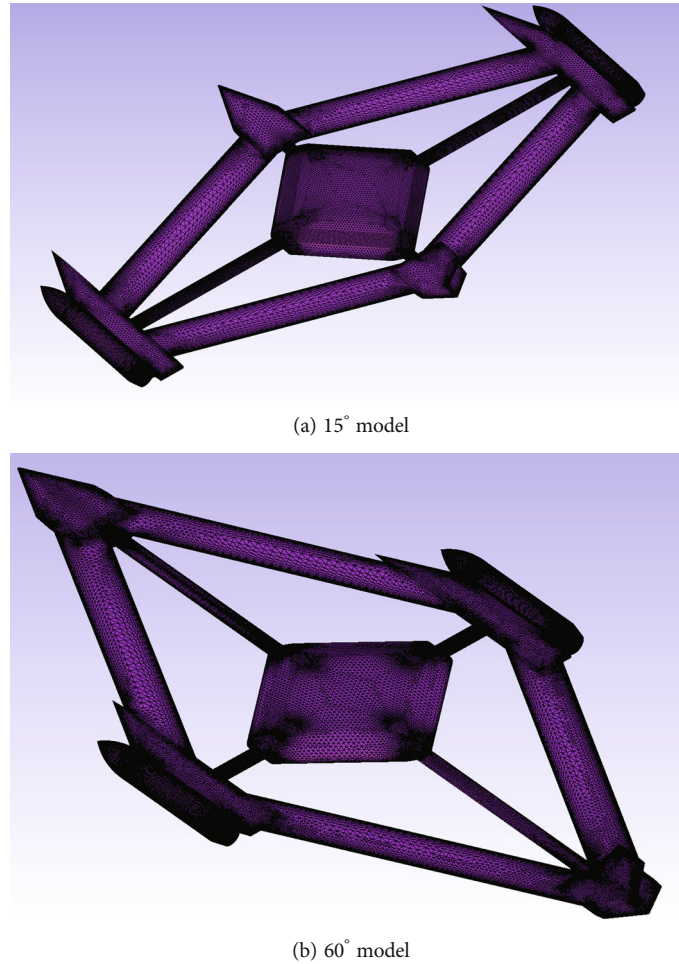
Figure 3: The wind tunnel test models.

(a) 15° model

(b) 60° model

FIGURE 4: Mesh of different models.

geometric center as the coordinate origin (0, 0, 0) and the direction along the fuselage axis as the x-axis and along the normal direction of the fuselage as the z-axis. The unit of measure for the coordinate system is millimeters. The moment reference points for the 15° sweep angle model and the 60° sweep angle model are $(-38.40, 0, 0)$ and $(-80.16, 0, 0)$.

The conventional variable swept aircraft has the following disadvantages: (1) the rotating mechanism of the wing is complex, and its size and weight are comparatively large; (2) the load of the rotating wing is concentrated on the pivot, which requires a greater design value of strength; and (3) the rapid deformation of the aircraft requires a powerful actuator [29, 30]. To verify the feasibility of the morphing method of the aircraft, we conducted a ground verification test of the morphing mechanism of the scaled-down model. We combined the configuration characteristics of the diamond joined-wing morphing aircraft to develop a new large-scale variant actuation mechanism design based on the "rack-type sliding rail" structure.

Figure 2 is the morphing verification vehicle. In the feasibility verification test of the morphing mechanism, we achieved the stepless variation of the front wing sweep between 15° and 60° and the engine tilt angle between 0°

and 90°, where the front wing and rear wing changes are completed within 10 s and the engine changes are completed within 5 s. In this paper's subsequent expressions, the sweep angle refers to the sweep back angle of the front wing.

3. Methodology

3.1. Wind Tunnel Test. The experimental test was carried out in the full test section of a high-speed wind tunnel in CARDC. The wind tunnel is a transonic-supersonic wind tunnel of semireflux type, and its size of the test section is $1.2 \, \text{m} \times 1.2 \, \text{m}$. The main performance is as follows: (1) Mach number range: 0.3~4.5 and control accuracy: 0.002; (2) Reynolds number range: $(0.47~9.57) \times 10^5$ Pa; (3) attack angle range: -20°~25° and control accuracy: 0.02°; and (4) side slip angle range: -12°~12° and control accuracy: 0.05°. Figure 3 shows two installation configurations of the aircraft. Due to the difference of the test Mach number, the test section was adapted for subsonic (Figure 3(a)) and the supersonic (Figure 3(b)) test conditions, respectively. The aerodynamic characteristics and control characteristics of the aircraft for different configurations have been obtained through wind tunnel tests.
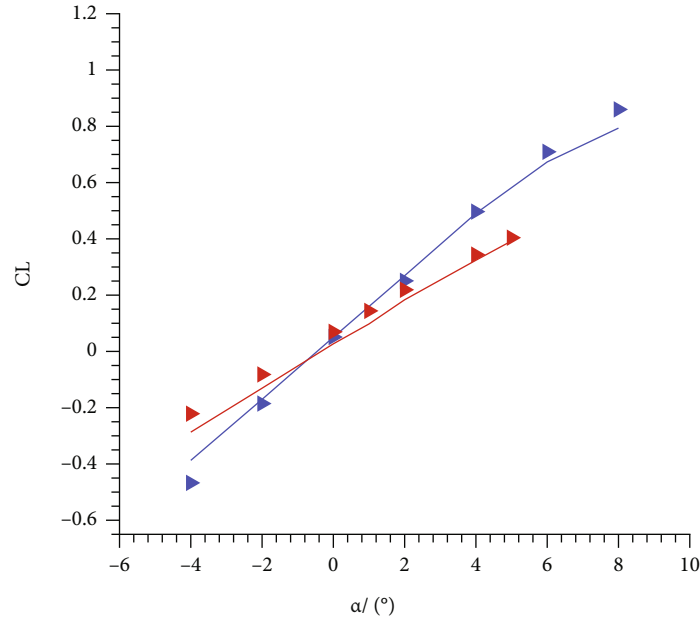
(a) The lift coefficient
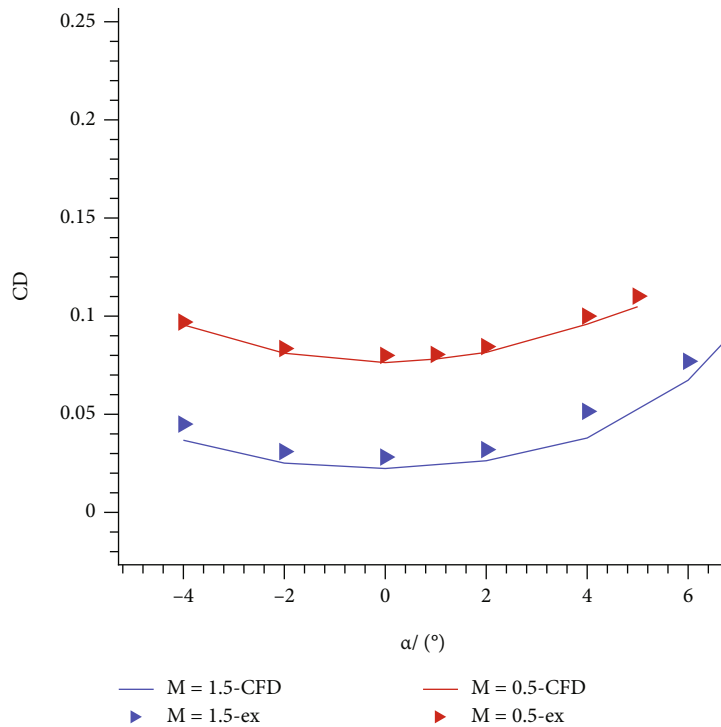
(b) Drag coefficient

FIGURE 5: Comparison of the CFD and test at $M = 0.5$ and 1.5.

The nominal Mach number for this test ranges from 0.3 to 1.5. The unique configuration of this aircraft determines the support type chosen for this wind tunnel test: ventral sting. Considering the balance's installation, the intermediate task module is thickened. Thus, in the following, we used a convenient and efficient CFD method to simulate the flows around the test model with ventral sting support, the test model without ventral sting support, and the original model,

respectively. The balance is connected with the ventral sting, which is fixed to the scimitar device. This test model has two states with the swept angle of the front wing as 15° and 60°, respectively.

The test adopts a six-component balance, with an uncertainty of measurement of 0.3%. For signal acquisition, the measured signals are digitally processed by an A/D converter, with a resolution of 18 bits and a comprehensive
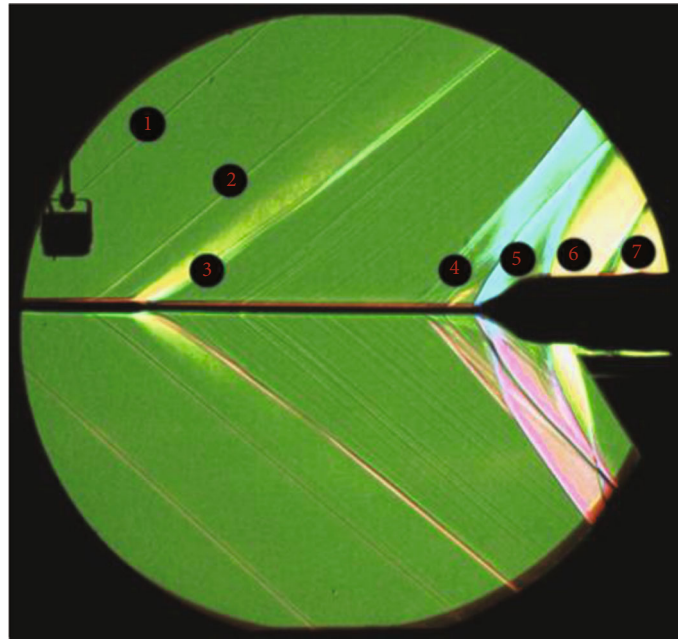
(a) The shock waves of different components tested by Schlieren
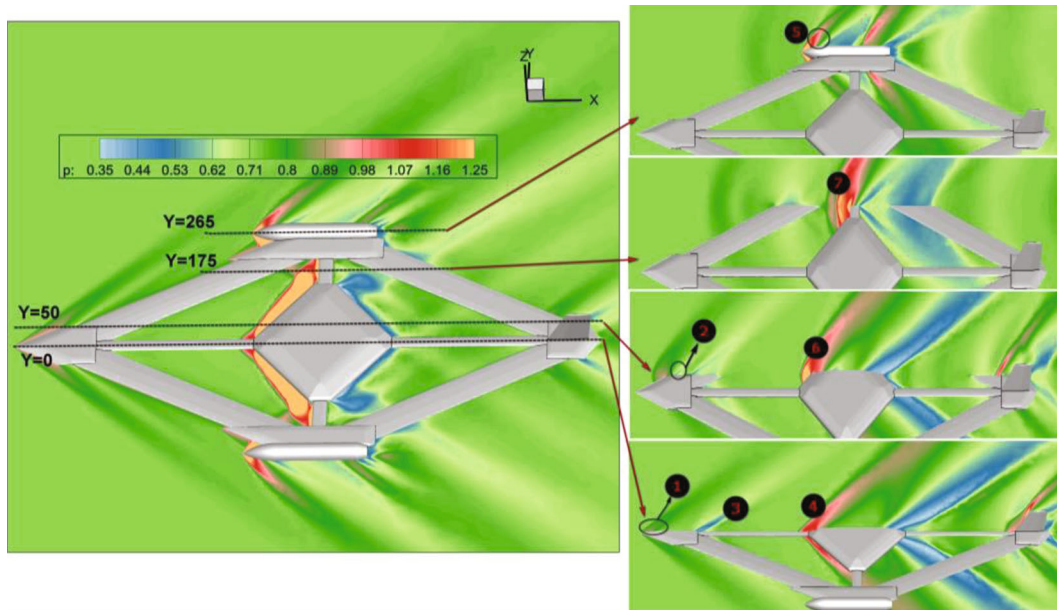
(b) The numerical result of the shock waves distribution for different components (the left is at $X = 0$; the right is at $Y = 0/50/175/265$)

FIGURE 6: Shock wave capture results of the test and numerical simulation at $M = 1.5$ and $\alpha = 0°$.

accuracy of 0.02%. The signal amplification range is adjustable from 1 to 8192 times. The general data processing platform software with preconfigured test parameters is used to calculate the test data. The pressure sensor is used to measure the pressure in the test. The main performance of the sensor is as follows: (1) total pressure sensor: Mensor CPT6100 absolute pressure sensor, range: $0 \sim 0.3$ MPa, $0 \sim 0.8$ MPa, and $0 \sim 2$ MPa and accuracy: 0.05%; (2) static pressure sensor: Mensor CPT6100 absolute pressure sensor, range: $0 \sim 0.15$ MPa and $0 \sim 0.5$ MPa and accuracy: 0.01%; and (3) pressure sensor at the bottom of the model: PPT

differential pressure sensor, range: + -20 psi and accuracy: 0.05%.

The experimental data are mainly corrected as follows: (1) the influence of the balance and the elastic angle of the strut on the model attitude is corrected, but the influence of the air deflection angle of the model is not deducted; (2) the influence of the misalignment of the balance calibration center and the model moment reference center is corrected; and (3) the influence of the weight of the model on the aerodynamic force is deducted, and the influence of the drag at the bottom of the model is not corrected.
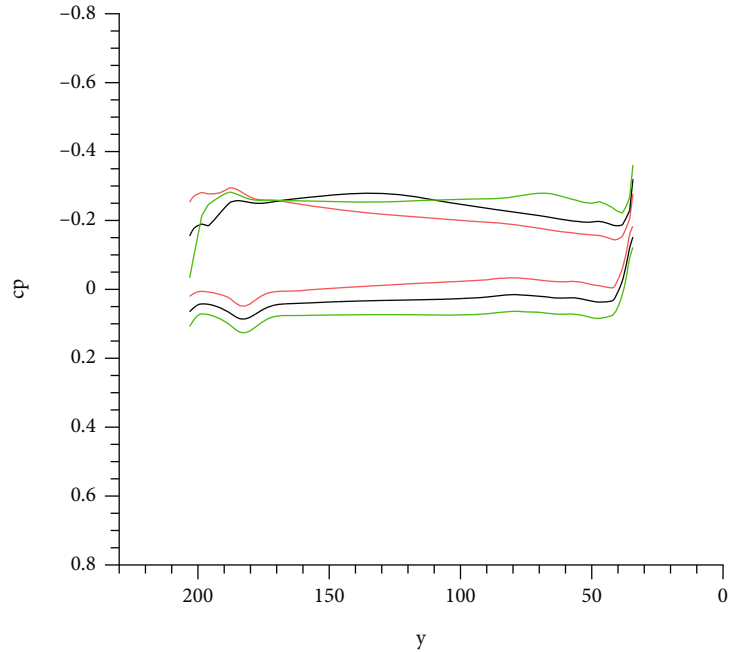
(a) Pressure distribution of the front wing at 1/2 chord
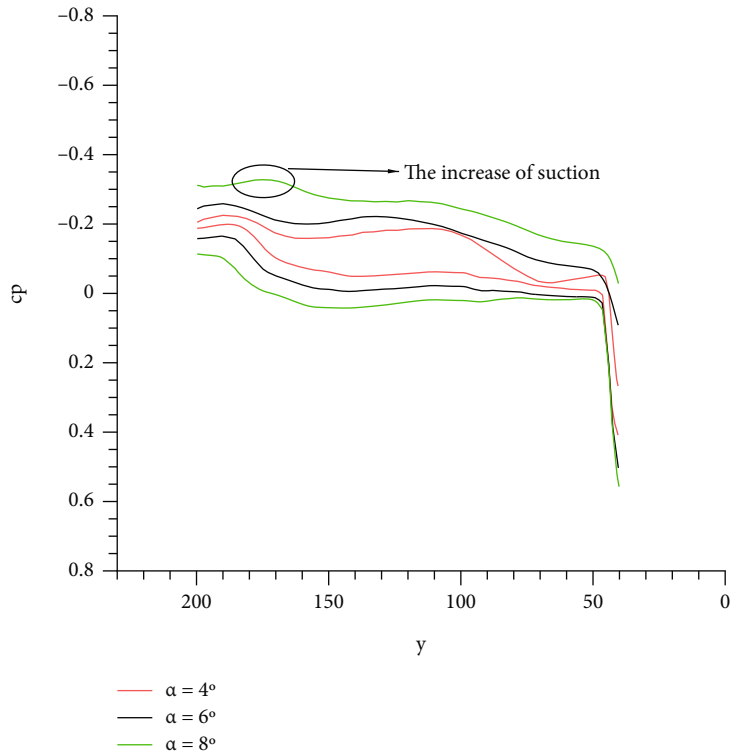
(b) Pressure distribution of the rear wing at 1/2 chord

Figure 7: Wingspan pressure distribution of the 60° model at M = 1.5 and α = 4°/6°/8°.

3.2. Numerical Simulation. The numerical simulation is carried out using an in-house solver NSM3D developed by CARDC, which is based on the finite volume method. The solver uses the compressible Navier-Stokes equations in conservative form as the control equation. The second-order upwind scheme is used for spatial discretization, and the dual-time stepping implicit method is used for time discretization. The Spalart-Allmaras [31, 32] model was chosen to close the equation system for the turbulent simulation, and some results are verified against the hybrid RANS-LES simulation [33]. The state of numerical simulation is free flight, and the grid computation domain is a sphere with a radius of 30 times the length of the model. The free flow Mach number range is 0.5~1.5; the inner boundary adopts the

nonslip solid wall condition, and the outer boundary adopts the free flow boundary condition.

The unstructured grids were created using the grid generation software Pointwise(Figure 4). Pointwise is a computational gridding software that launched its first version in 2008, formerly known as Gridgen. Gridgen's development was funded by the U.S. Air Force, NASA Langley, and the Ames Research Center. The version number of Pointwise software used in this work is V18.2 R2. For the 15° model, the value of $y+$ is 60, and the number of grid cells is about 21 million. For the 60° model, the value of $y+$ is 10, and the number of grid cells is about 34 million. The cell type of surface mesh is the triangle, and the growth rate of the T-Rex on the leading edge of the wing is 1.3. The cell type of block includes pyramids, prisms, and hexes, which are automatically generated by Pointwise. The maximum layer of T-Rex is 50 and the growth rate of T-Rex is 1.3. The subsonic calculation time step is 7000, and the data converge at about 1500. The time step of the supersonic calculation is 5000 steps, and the data converge at about 1000 steps.

4. Results

4.1. Comparison between CFD Results and Test Results. Figure 5 shows the aerodynamic coefficient of the 15° sweep angle model at $M = 0.5$ and the 60° sweep angle model at $M = 1.5$. The difference in the lift coefficient curve between the test and the numerical simulation is slight. Despite that the drag coefficient is slightly lower than the test results due to the fact that the numerical simulation does not consider the interference from tunnel wall and the elastic deformation, the calculation results are seen to be consistent with the wind tunnel test results, proving the reliability of the numerical calculation method used.

Figure 6 shows the shock wave structures captured by the test [34] and numerical simulation at $M = 1.5$, where the p is a dimensionless parameter ($p = p/\rho_\infty a_\infty^2$, (the subscript ∞ corresponds to the value of external flow). Using the numerical simulation, we can analyze the positions of the shock waves in different components of the aircraft, and the same number corresponds to the same shock. We can see that oblique shock waves appear at the leading edge of the nose and the leading edge of the task module to slow down and pressurize the flow, while expansion waves appear at the trailing edges of the task module and the engine. In addition, it is found that there exists a low-pressure region behind the task module outer edge (Figure 6(b)), which is another reason for the increase in lift in the outer section of the rear wing in subsequent analysis (Figure 7(b)). From the shock capture results, the pressure changes of numerical simulation are in good consistency with the shock position of the test.

4.2. Aerodynamic Characteristics at Typical Conditions. This part will present the typical aerodynamic results for the diamond joined-wing morphing aircraft. Table 2 shows the numerical simulation parameters for the 15°model and 60° model.

TABLE 2: Parameter space of the numerical simulation for the 15° model and 60° model.

Λ (°)	M	Ler	P_0 (Pa)	Re
	0.3	0.052326	98000	348870
15	0.5	0.052326	101222	560870
	0.75	0.052326	110000	905050
	0.75	0.100988	110000	1553740
60	0.9	0.100988	114466	1671890
	1.2	0.100988	128656	2001320
	1.5	0.100988	139062	2093940

Figure 8 shows the aerodynamic characteristics of the two configurations with different values of the sweep angle. For the 15° model, the lift coefficient and drag coefficient remain nearly unchanged with increasing M. For the 60° model, it is found that the freestream speed has a more significant effect. The slope of the lift coefficient curve increases with increasing M for the subsonic case. The change rules of the drag coefficient curves for different speed domains are the same, and the maximum drag coefficient is at $M = 1.2$. The maximum lift-to-drag ratio is about 13.5 at $M = 0.5$ and $\alpha = 4°$, 12.8 at $M = 0.75$ and $\alpha = 4°$, and 3.4 at $M = 1.5$ and $\alpha = 6°$. For the 15°model, the pitching moment coefficient is statically unstable in the range of small angle of attack, and to which, the Mach number has little influence. When $\alpha > 4°$, it becomes statically stable, and the absolute value of the slope increases with the increase in the incoming Mach number.

Figure 9 shows the comparison of the lift-to-drag between the diamond joined-wing configuration and the Firebee aircraft at different sweep angles (the data of Firebee studied by Yan [35] is about subsonic and transonic states). BQM-34 Firebee UAV can fly as fast as Mach 0.97 and at altitudes as high as 18.29 km (60,000 ft). In this work, two configurations, dash (sweep angle of 60°) and cruise (sweep angle of 15.97°), are chosen as the benchmark. Wing parameters of the two configurations are shown in Table 3.

For the 15° model, the maximum lift-to-drag of diamond joined-wing configuration is about 13.5 at $M = 0.5$ and $\alpha = 4°$, and that of the Firebee aircraft is about 15.1 at $M = 0.5$ and $\alpha = 4°$. Nevertheless, the maximum lift-to-drag model is significantly better than that of the Firebee aircraft at the transonic state. For the 60° model, the difference between the lift-to-drag curves of the two configurations is small at the transonic state. Comparing the research results of Lv et al. [11] (Figure 10), the difference of the maximum lift-to-drag ratio is small at $M < 0.8$, and in the test Mach number range, the maximum lift-to-drag ratio is at about $M = 0.5$, which is similar to the diamond joined-wing morphing configuration. On the whole, the diamond joined-wing morphing aircraft has good supersonic aerodynamic characteristics while ensuring subsonic and transonic aerodynamic performance.

We compared the aerodynamic characteristics of the cross-speed domain at $\alpha = 4°$ with a variable-sweep Blend-

(a) Lift coefficient

(b) Drag coefficient

(c) Lift-to-drag ratio
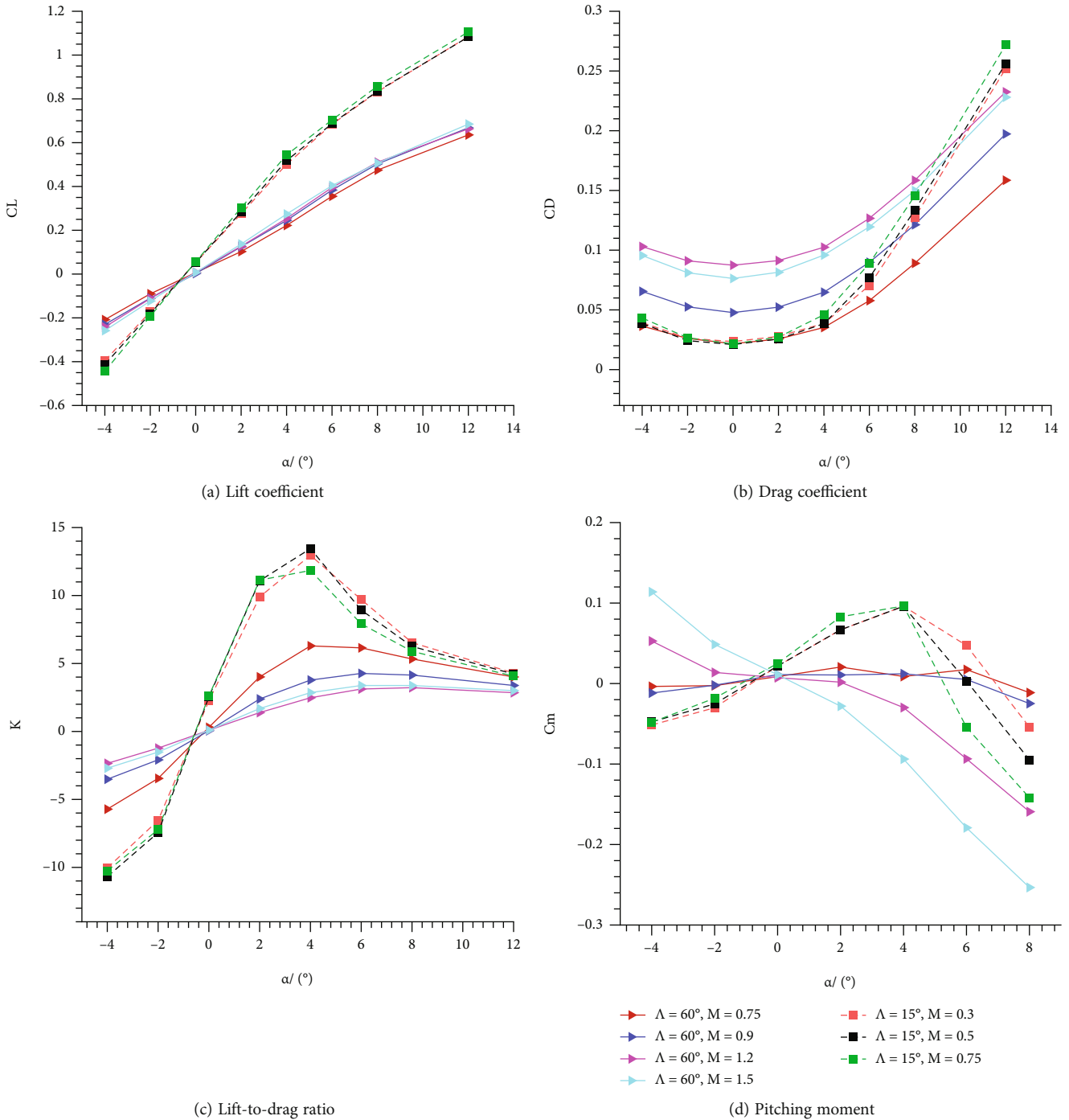

(d) Pitching moment

FIGURE 8: Typical aerodynamic characteristics of the 15° model and 60° model at different Mach numbers.

Wing Body (BWB). The reason for choosing the 4° angle of attack is that the maximum lift-to-drag ratio is generally obtained near it [36]. The data of BWB is studied by Chen et al. [37], mainly for the two typical states of 0° and 60°. There are two morphing ways of BWB that have been studied: rotating and shearing. From the comparison in Figure 11, the main advantage of the diamond joined-wing aircraft is that it has better subsonic lift characteristics at $\Lambda = 15°$. The lift characteristic curve of diamond joined-wing configuration can maintain a good linear growth

from subsonic acceleration to transonic states. Still, the lift characteristic of BWB configuration has a significant drop near $M = 0.7$. The value of the lift coefficient has improved by about 62% at $\alpha = 4°$ and $M = 0.5$, which means better capabilities of short take-off and landing and less fuel consumption at cruise. In the state of a high aspect ratio, the four wings of diamond joined-wing configuration provide more lift. Although the drag coefficient has also increased, this does not affect its excellent lift-to-drag ratio at subsonic and transonic speeds.
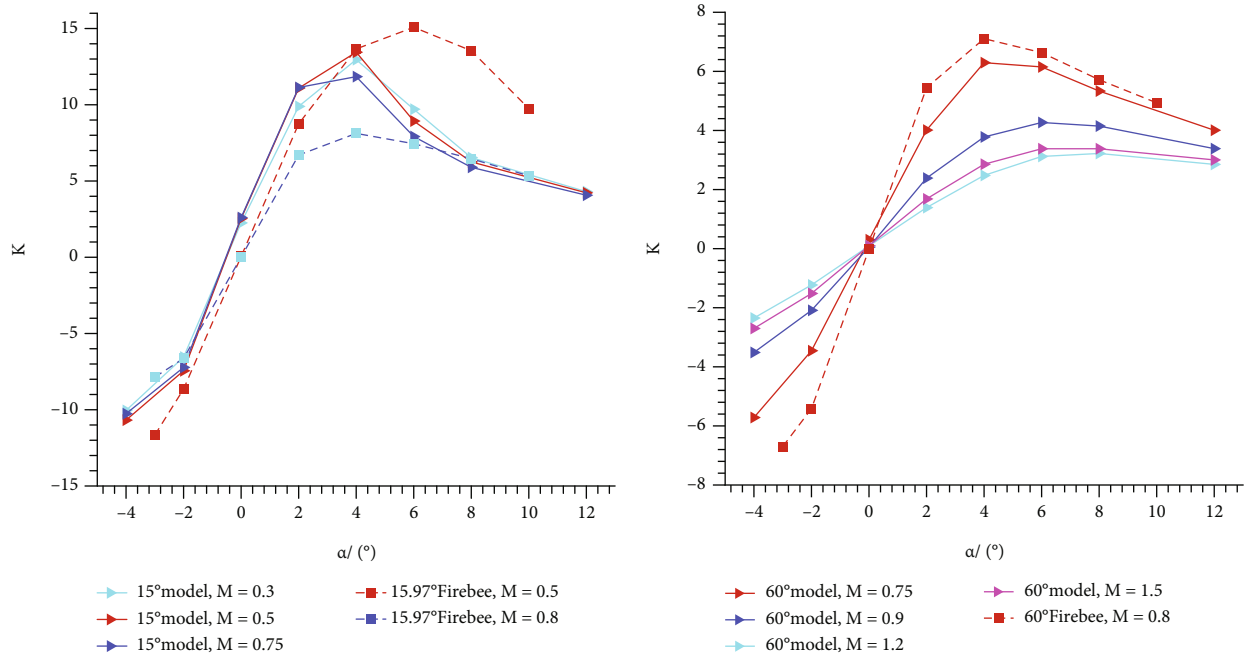
(a) The lift-to-drag ratio of the 15° model at subsonic and transonic

(b) The lift-to-drag ratio of the 60° model at transonic and supersonic

FIGURE 9: The lift-to-drag ratio of the diamond joined-wing configuration and the Firebee aircraft [33].

TABLE 3: Wing parameters of two configurations.

Λ (°)	Root chord (m)	Tip chord (m)	Span (m)	Mean aerodynamic chord, L ref (m)	Wing area, S ref (m^2)
15.97	0.878	0.341	6.802	0.688	4.500
60	2.397	0.286	3.842	1.935	5.765
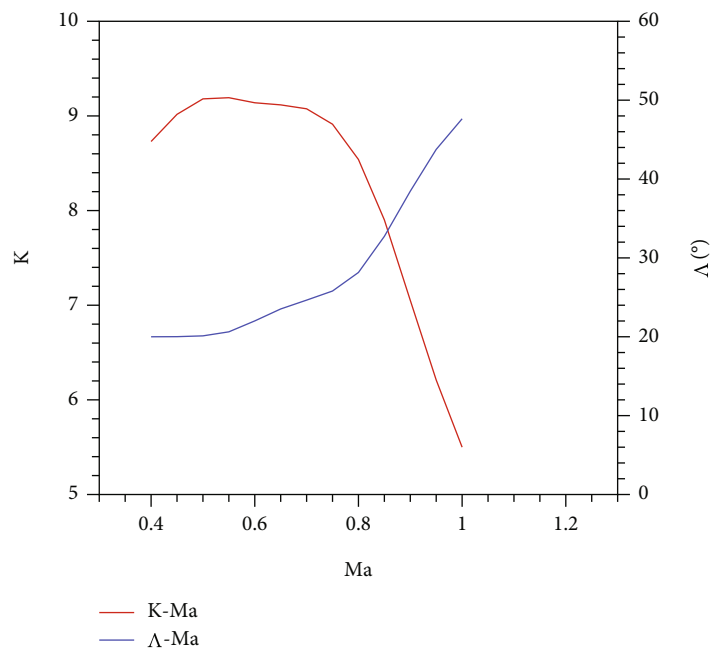
FIGURE 10: The best rule of the optimal variable sweep wing studied by Lv et al. [11].

(a) Lift coefficient

(b) Drag coefficient

(c) Lift-to-drag ratio
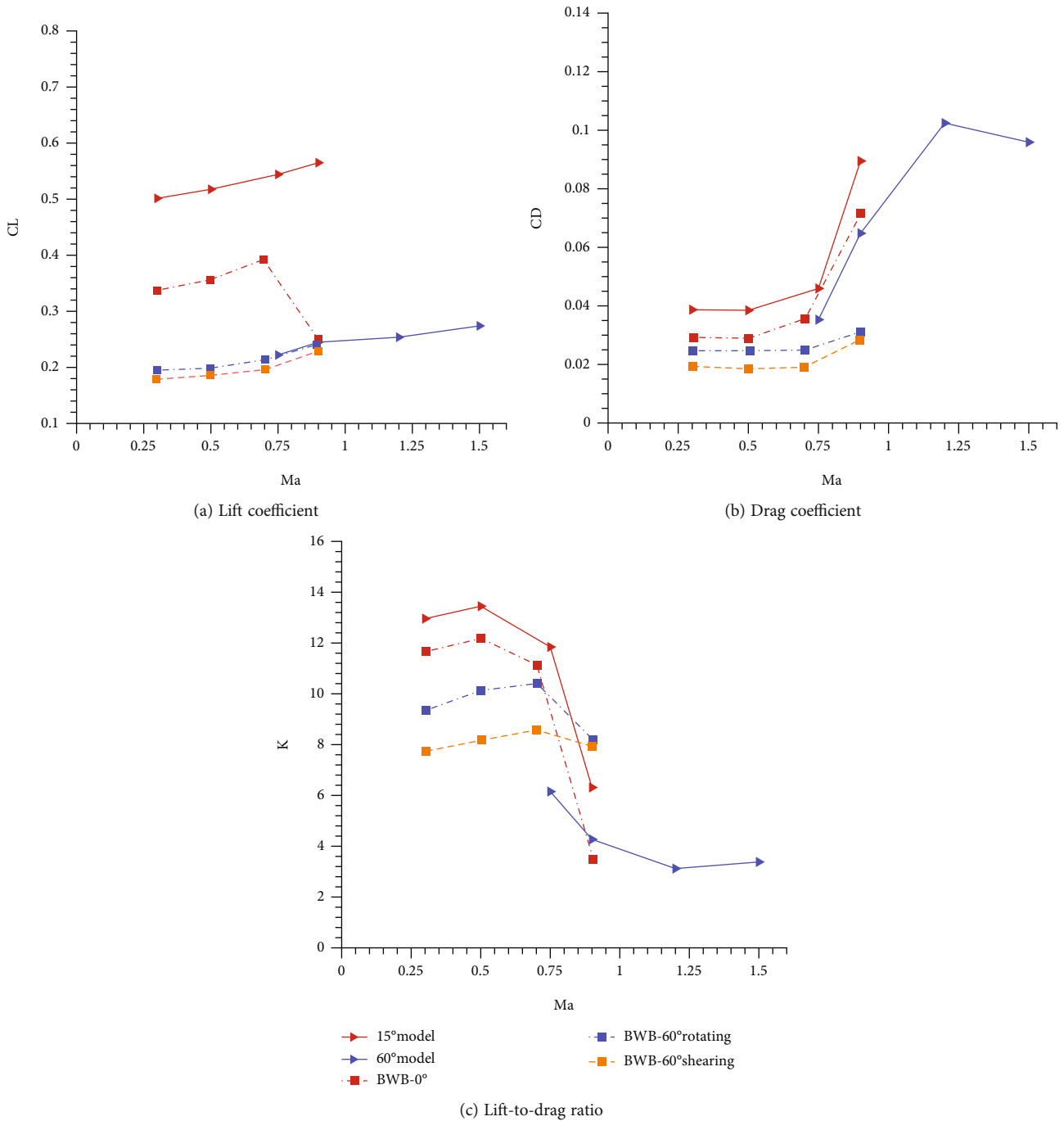
Figure 11: Aerodynamic characteristic comparison of morphing diamond joined-wing configuration and variable sweep BWB at different Mach numbers and $\alpha = 4°$ [35].

Due to the configuration limitation and the research purpose, the paper does not give the supersonic aerodynamic characteristics of the variable-sweep BWB configuration. For a simple comparison, the lift characteristic of the 60° model is the same as the BWB at transonic speed, but there is a greater drag.

Liu and Wang have studied a variable forward-swept configuration; by adjusting the forward sweep angle, the aircraft has three configurations: straight wing, forward-swept wing, and the delta wing configuration [38] (Figure 12).

Figure 13 shows the comparison of maximum lift-to-drag and zero-lift drag between the morphing diamond joined-wing configuration and the variable forward-swept configuration. The two configurations have similar maximum lift-to-drag ratios at subsonic, transonic, and supersonic speeds, especially in the sprint phase at $M = 1.5$. The value of zero-lift drag is also identical at transonic and subsonic speeds. The performance of penetration at high speed is mainly affected by the drag characteristic, especially the drag of supersonic shock waves. Figure 13(b) shows that

(a) Straight wing configuration

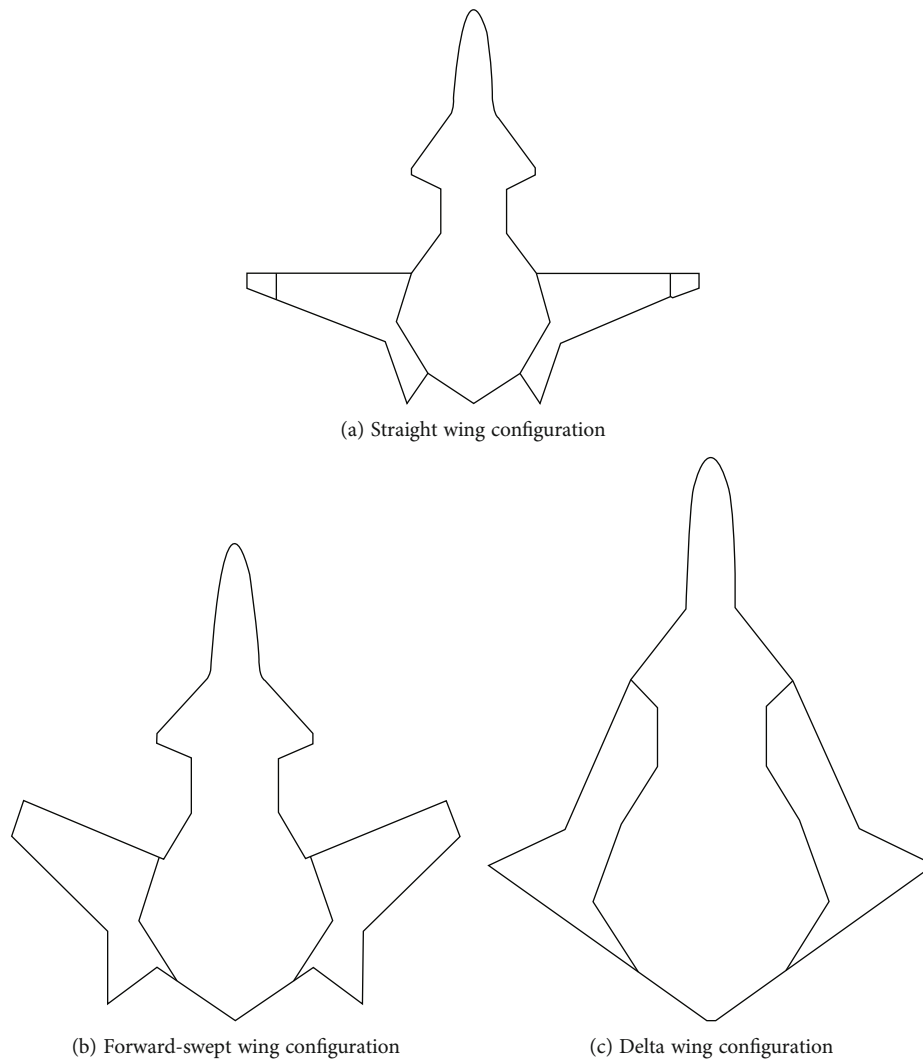(b) Forward-swept wing configuration

(c) Delta wing configuration

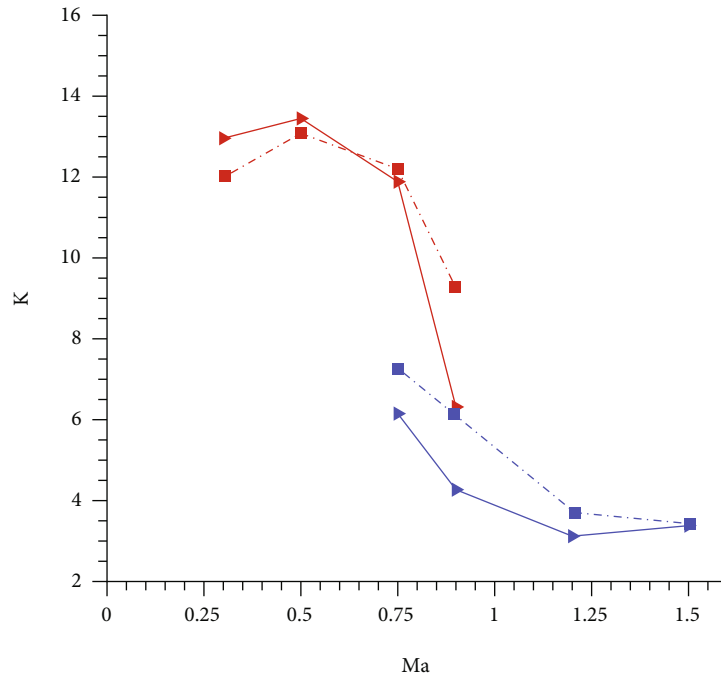FIGURE 12: Variable forward-swept configurations.

the zero-lift drag of the diamond joined-wing configuration has decreased about 60% than the delta wing configuration, which means better sprint performance and lower fuel consumption.

4.3. Aerodynamic and Interference Characteristics of the Front Wing and the Rear Wing for the 15° Model. According to the configuration features of the aircraft, we have conducted a subsequent analysis on the aerodynamic characteristics of two main components, i.e., the front and rear wings. Figure 14(a) shows the lift characteristics of the front and rear wings of the 15° model. In the linear segment ($\alpha < 4°$), the lift coefficient curves under different Mach numbers nearly coincide for both the front wing and rear wing. But the lift coefficient slope of the rear wing is significantly smaller than that of the front wing. The reason is that the rear wing is located in the wake of the upstream components, and the rear wing produces upwash on the front wing (increasing the effective angle of attack and thus increasing the lift), whereas the front wing produces downwash on the rear wing, reducing its angle of attack and the consequent lift. The trends of lift coefficients of

the front wing and the rear wing change significantly at $\alpha > 4°$; i.e., the lift coefficient slope for the front wing decreases, and the slope for the rear wing increases slightly. The main reasons for this change include the flow separation on the upper wing surface and the development of wingtip vortices.

All four wings have the same area, so we analyze another value: "the aerodynamic force ratio of the front wing to that of the rear wing." As α increases, the interference effects of the task module and the telescopic support rod on the rear wing decrease, and the specific values tend to be the same, reaching about 1.3 at $\alpha = 12°$ (Figure 14(b)). The rear wing lift contribution is significantly higher than another Mach number at $\alpha > 4°$ and $M = 0.75$. Of course, the difference in lift characteristics is partly due to the difference in sweep angle between the front and rear wings.

As shown in Figure 15, the drag coefficient curves of the front and rear wings of the 15° model vary with M in the same way. Like the lift coefficient curves, an inflection point appears at $\alpha = 4°$ for drag curves. That is, the rear wing drag is greater than that of the front wing when $\alpha < 4°$ and the drag of the front wing increases sharply at $\alpha > 4°$. The

(a) Maximum lift-to-drag ratio
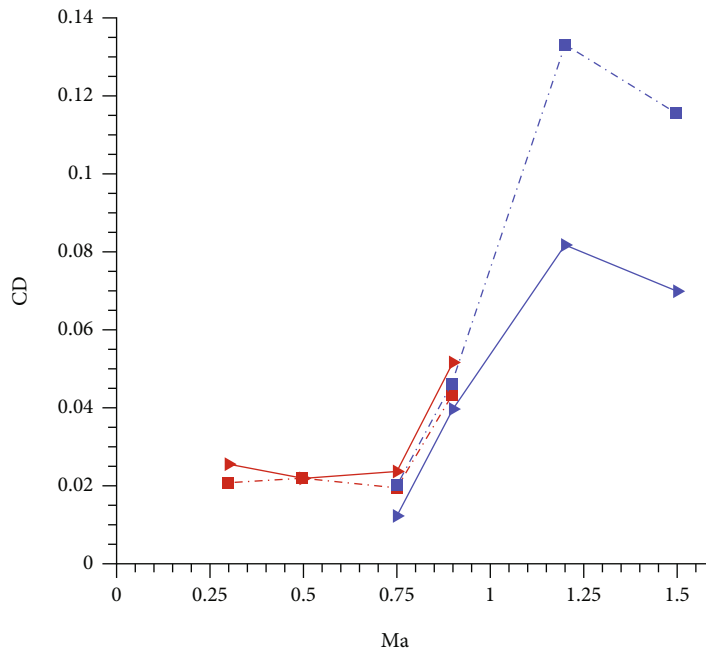
(b) Zero-lift drag

FIGURE 13: Aerodynamic characteristic comparison of morphing diamond joined-wing configuration and variable forward-sweep wing configuration at different Mach numbers [33].

specific value fluctuates around 0.5 at $\alpha < 4°$, and it becomes about 1.5 when $\alpha > 4°$. Considering the pitching moment characteristics of the 15° model, the differences in aerodynamic characteristics between the front wing and rear wing at different α can affect the pitching attitude of the aircraft (Figure 8(d)). Nevertheless, it can also be understood that

the reasonable coordination of the front wing rudder surface and rear wing rudder surface can produce better control efficiency.

Figure 16 shows the surface streamline pattern, the volume streamlines, and the c_p_distribution at wings for the 15° model. At low speeds, the maximum lift-drag ratio
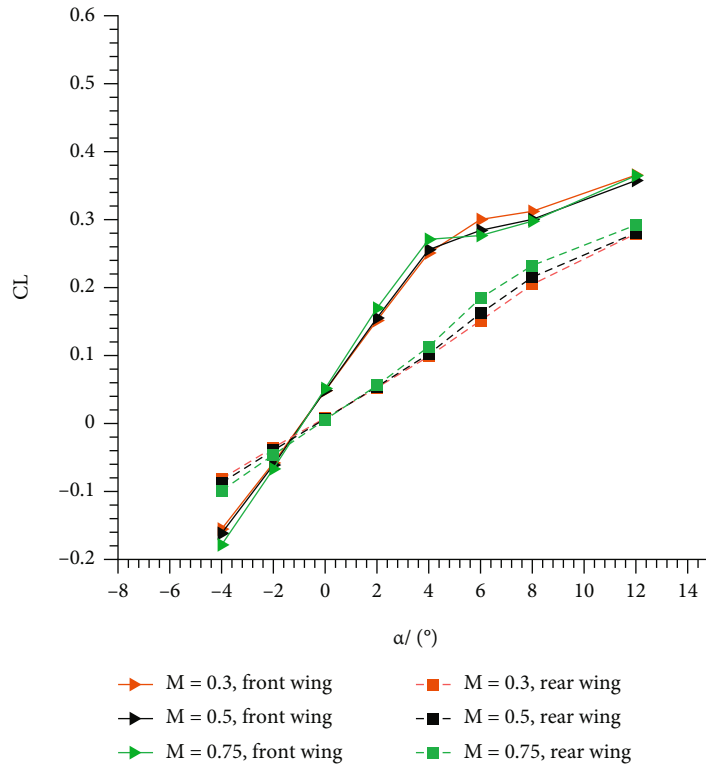
(a) Lift coefficient of front wings and rear wings
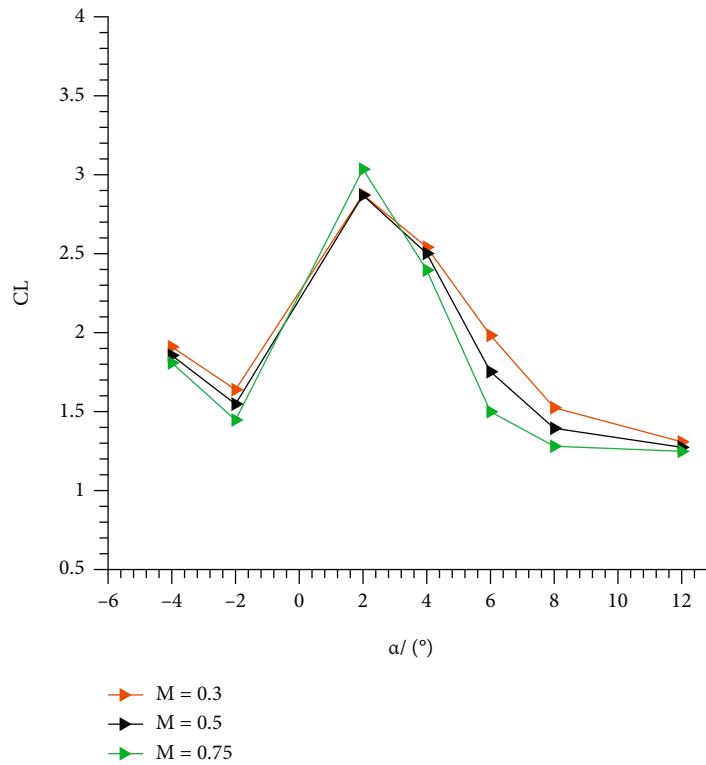
(b) Ratio of lift between front wings and rear wings

FIGURE 14: Lift characteristics of wings of the 15° model.

is usually located at $\alpha = 4°$. In this condition, the upper surface of the front and rear wings exhibits strong attached flow at each flight speed. The four wings provide the aircraft with a greater lift surface. Therefore, compared to the morphing aircraft with the traditional configuration, the diamond-joined wing aircraft has better

(a) Drag coefficient of front wings and rear wings
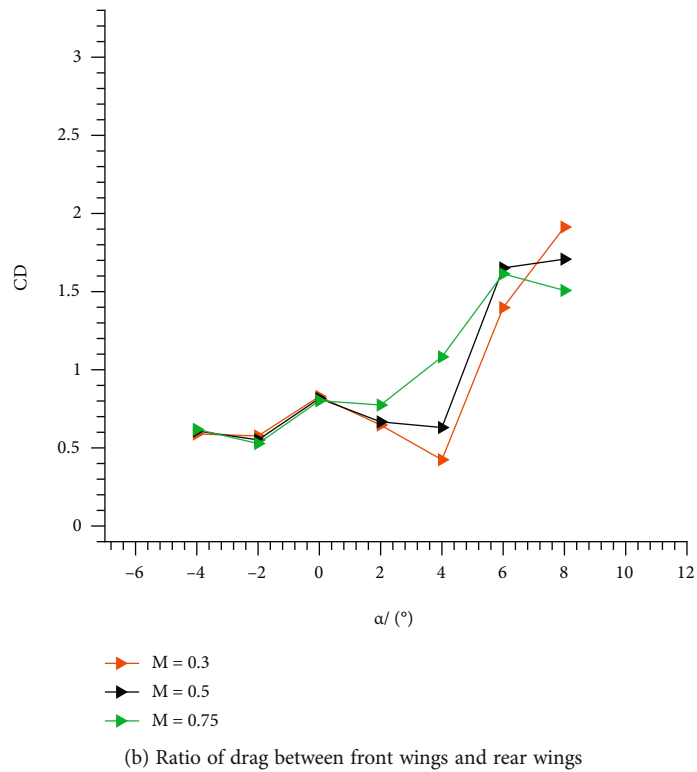

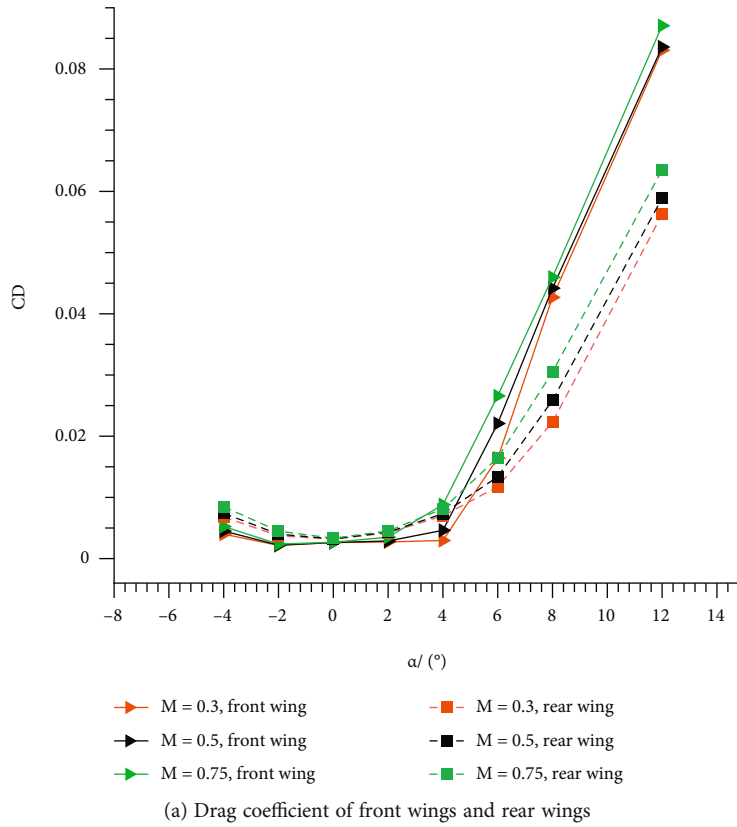(b) Ratio of drag between front wings and rear wings

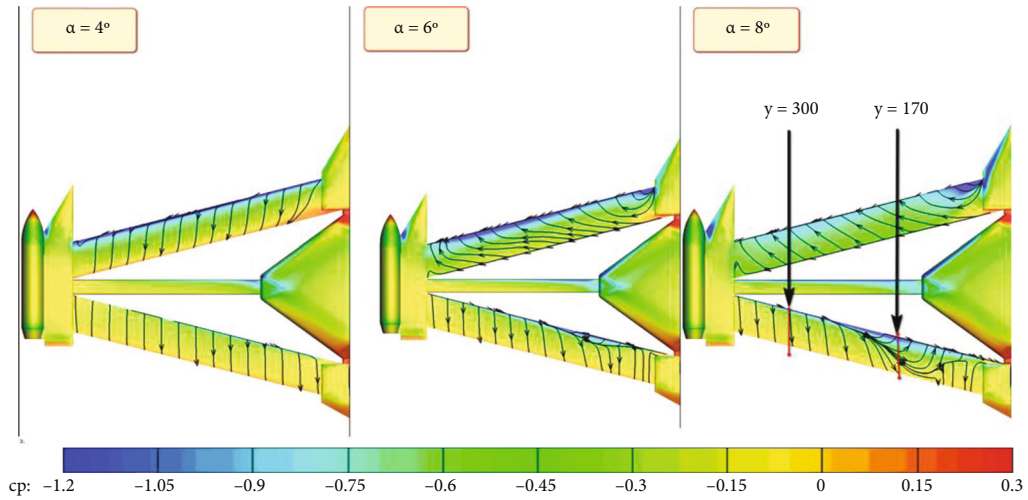FIGURE 15: Drag characteristics of wings of the 15° model.

lift-drag characteristics at low speeds, especially transonic speeds [35, 37].

The flow at the leading edge of the front wing begins to separate locally, and the attachment line is at about 30%
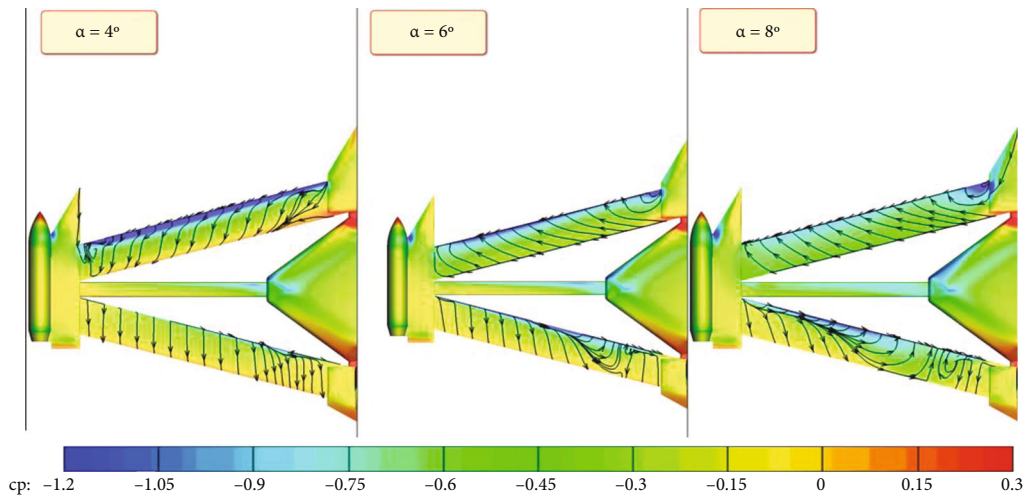
chord of the root at $M = 0.3$ and $\alpha = 6°$. The existence of separation bubble increases the suction at the leading edge of the front wing, and due to the effects of the swept angle, the trailing edge of the front wing exhibits strong spanwise
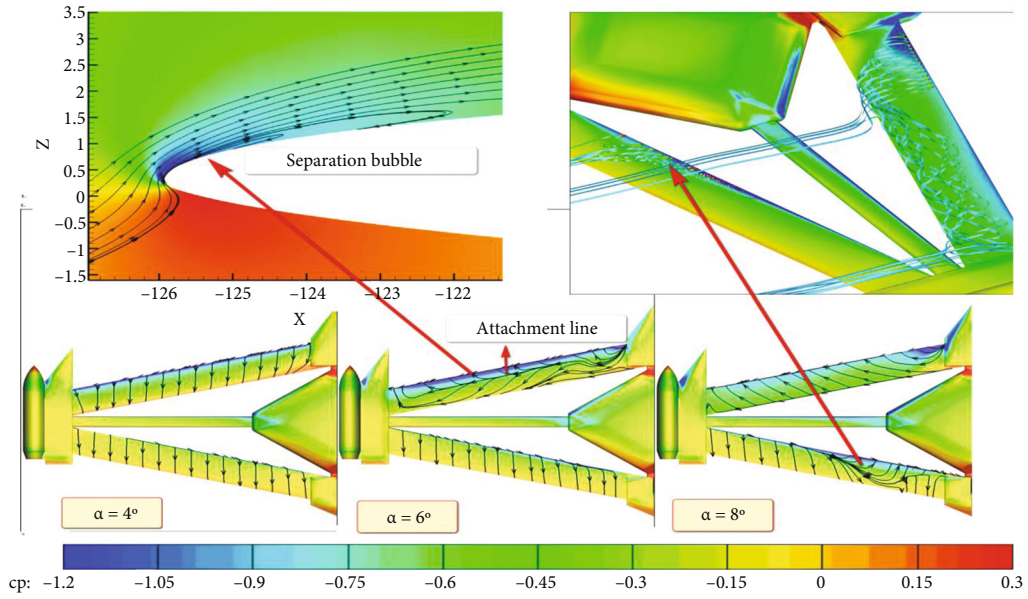
(a) The flow characteristics of the 15° model at $M = 0.3$ and $\alpha = 4°$, 6°, and 8°

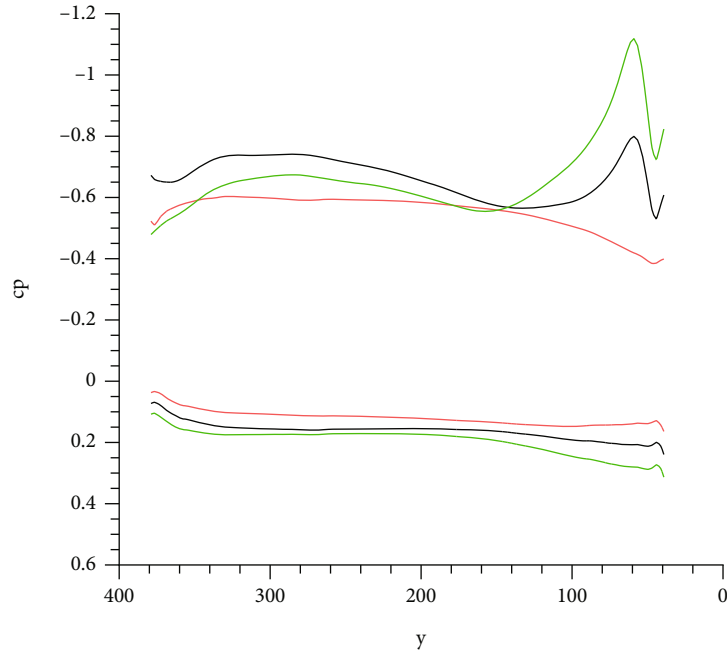(b) The flow characteristics of the 15° model at $M = 0.5$ and $\alpha = 4°$, 6°, and 8°

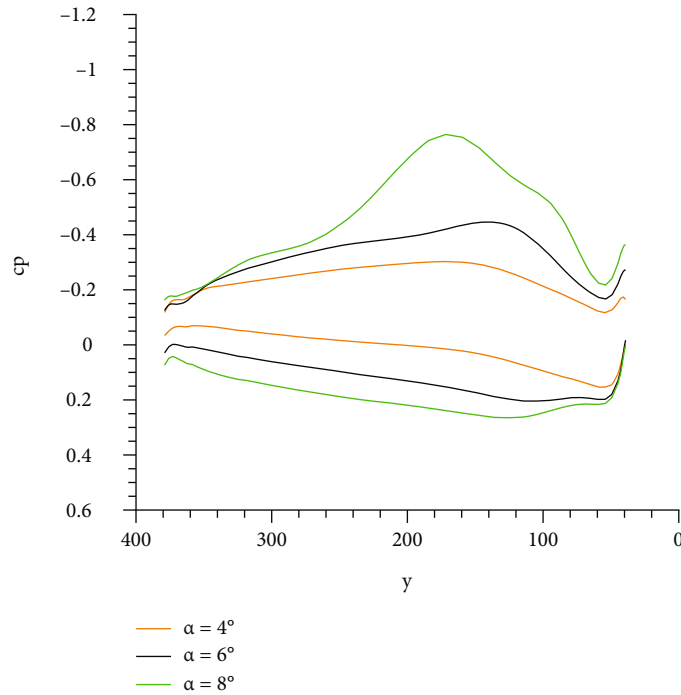

(c) The flow characteristics of the 15° model at $M = 0.75$ and $\alpha = 4°$, 6°, and 8°

FIGURE 16: Surface streamline, volume streamline, and c_p_distribution at wings for the 15° model, at $M = 0.33/0.5/0.75$.

(a) Pressure distribution of the front wing at 1/4 chord

α = 4°
α = 6°
α = 8°

(b) Pressure distribution of the rear wing at 1/4 chord

FIGURE 17: Wingspan pressure distribution of the 15° model at $M = 0.5$.

flow. With the increase in α, the airflow on the front wing surface becomes countercurrent at $\alpha = 8°$. The appearance of these separations is also the main reason for the gradual decrease in the lift slope of the front wing with α.

Moreover, the leading edge vortex of the front wing root expands and moves along the trailing edge with the increase in the M and α (Figure 16(a)). Since a vortex similar to the wingtip vortex is formed at the outer edge of the task module, the first location where the rear wing separates is behind

the outer edge of the task module rather than the wing root, enhancing the suction at the upper wing surface of the inner section of the rear wing (Figure 17(b)). At $y = 300$, the spanwise flow weakens, and less interference from the fuselage is observed, so the upper surface pressure changes slightly.

Compared with the UAV studied by Sun [39], the connecting bracket of the winglet acts like a winglet, avoiding the wingtip vortex caused by the pressure difference between the upper and lower surface of the wing
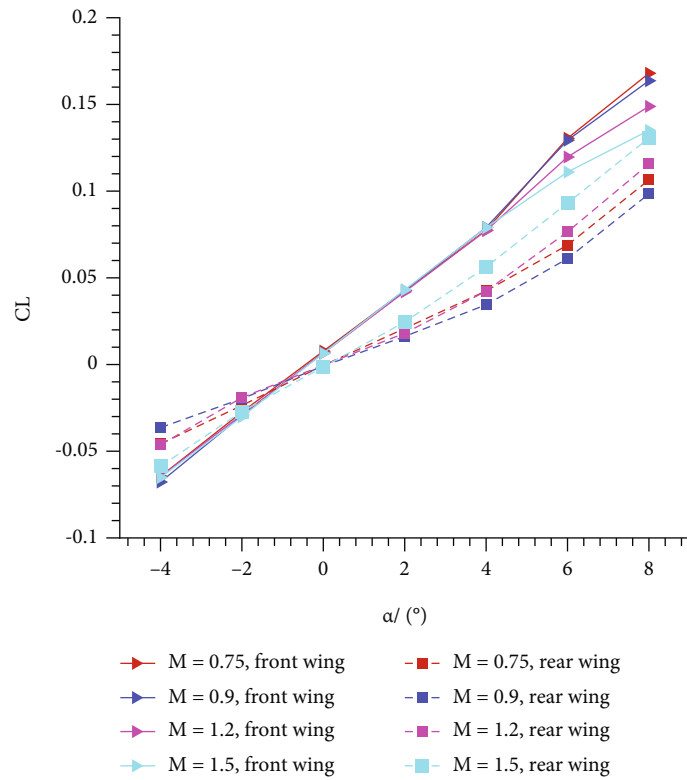
(a) Lift coefficient of front wings and rear wings
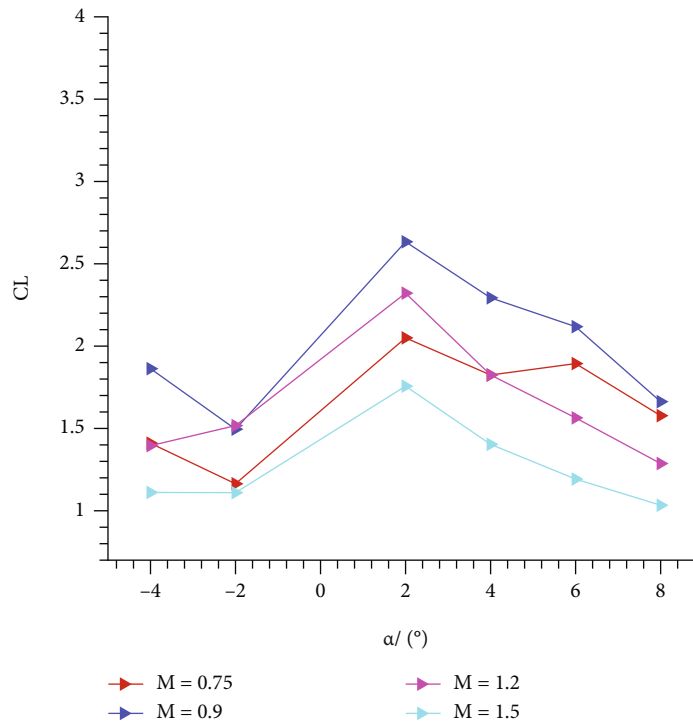
(b) Ratio of lift between front wings and rear wings

FIGURE 18: Lift characteristics of wings of the 60° model.

[40], which shows a noticeable decrease in the lift on the tip of the rear wing. So there is still a good pressure difference at the wingtip to provide lift. Due to these flow field phenomena, the aircraft's lift characteristic have been enhanced in the subsonic state. Moreover, the wing separation, which develops from the wing span's root, becomes more severe with increasing M at the same α.
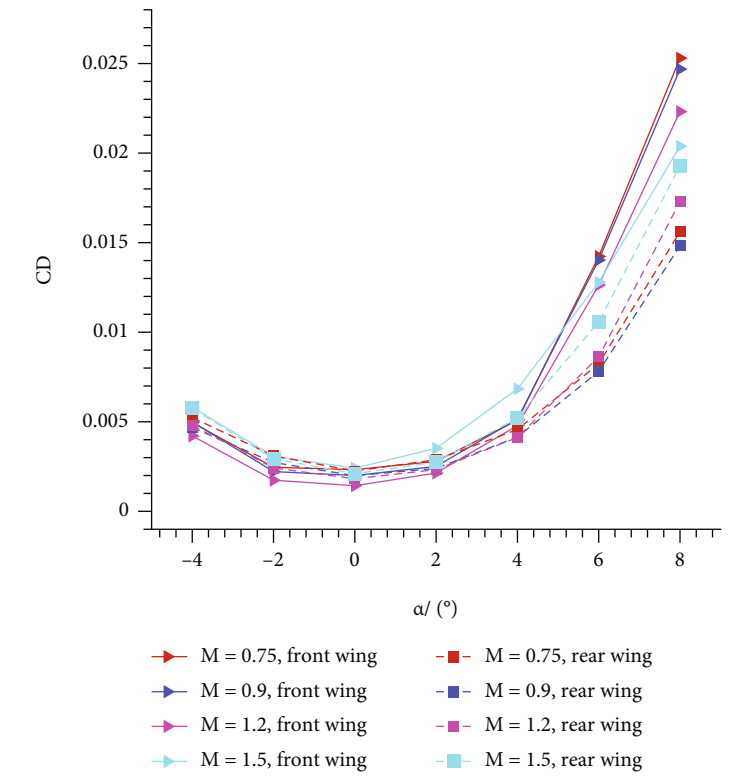
(a) Drag coefficient of front wings and rear wings
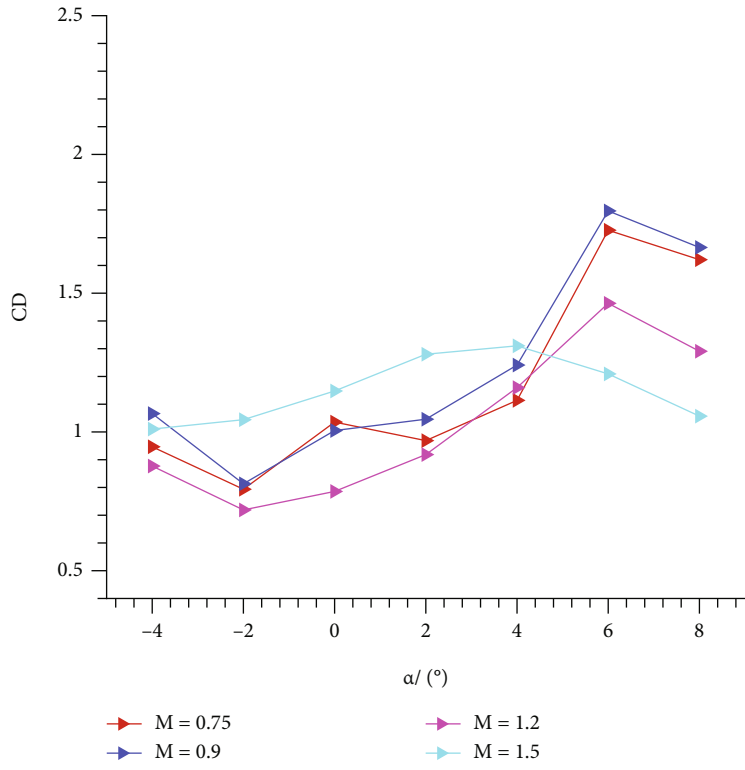
(b) Ratio of drag between front wings and rear wings

FIGURE 19: Drag characteristics of wings of the 60° model.

4.4. Aerodynamic and Interference Characteristics of the Front Wing and the Rear Wing for the 60° model. Compared with the low-speed model (15° model), the distance between the front and rear wings with a sweep angle of 60° becomes larger, reducing the aerodynamic interference to the rear wing, so the lift ratio of the rear wing is significantly greater
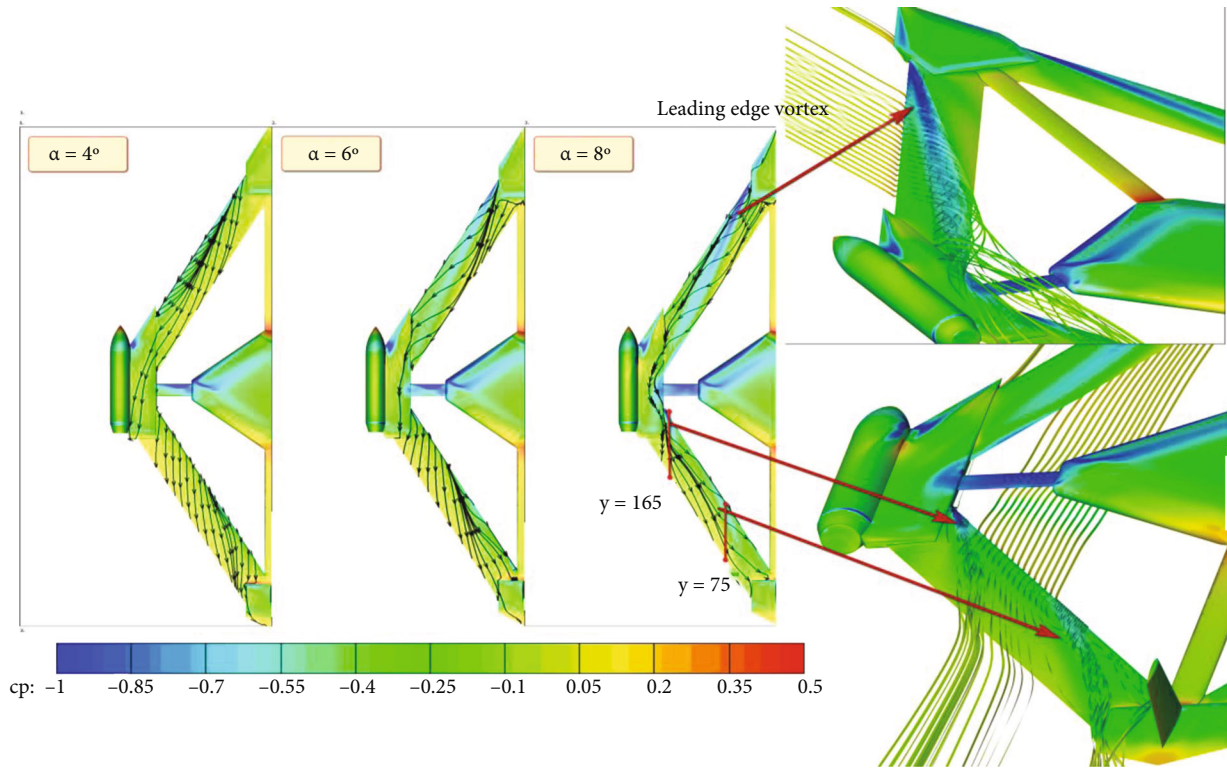
(a) The flow characteristics of the 60° model at $M = 0.75$

(b) The flow characteristics of the 60° model at $M = 1.5$

FIGURE 20: Surface streamline, volume streamline, and c_p_distribution at wings for the 60° model, at $M = 0.75/1.5$.

than that of the 15° model (Figure 18). The ratio of lift between front wings and rear wings is basically the same, but there is a significant difference in magnitude.

As shown in Figure 18(a), the lift coefficients of the front wing show noticeable differences at $\alpha > 4°$, especially at the supersonic stage. In the calculating angle of attack range, the rear wing lift is strongly correlated with the Mach num-
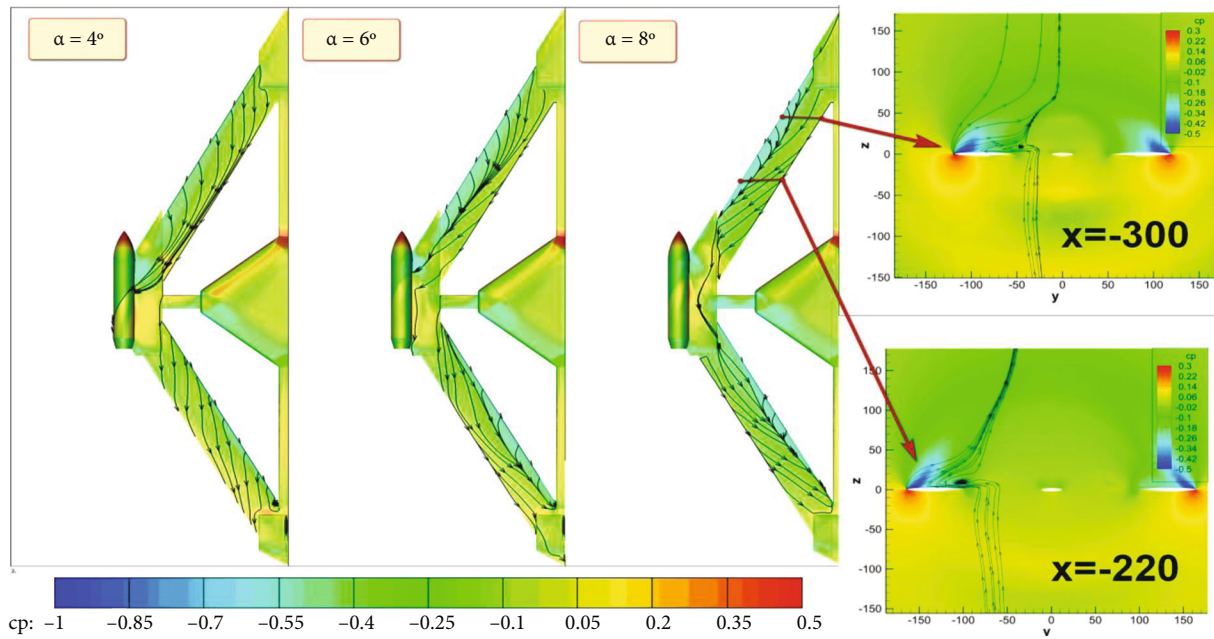
ber. The difference with the 15° model is that the slope of the lift coefficient curve of the front wing increases at $\alpha > 4°$ and that of the rear wing increases at $\alpha > 6°$. The change rule of the ratio of aerodynamic contribution is the same at different Mach numbers. Nevertheless, compared with other velocities, the complex transonic flow results in a significant difference in the lift ratio between the front and rear wings,
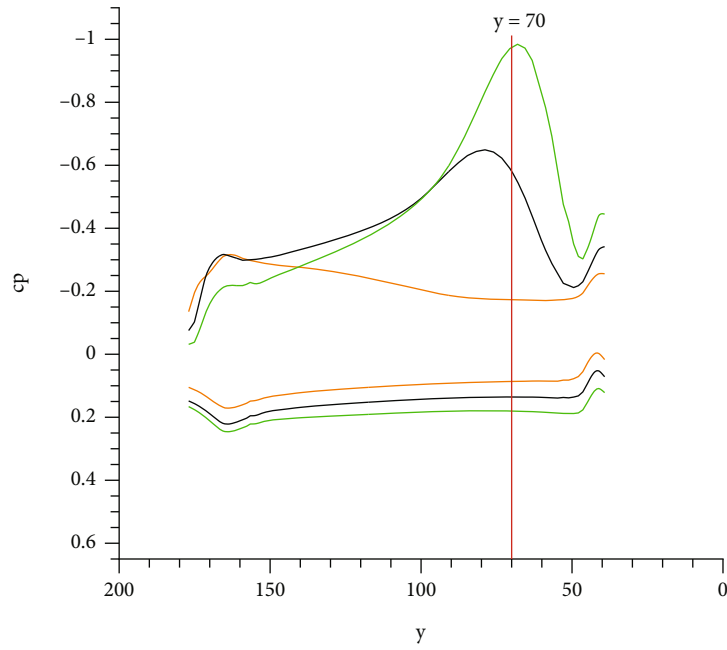
(a) Pressure distribution of the front wing at 1/4 chord

α = 4°
α = 6°
α = 8°
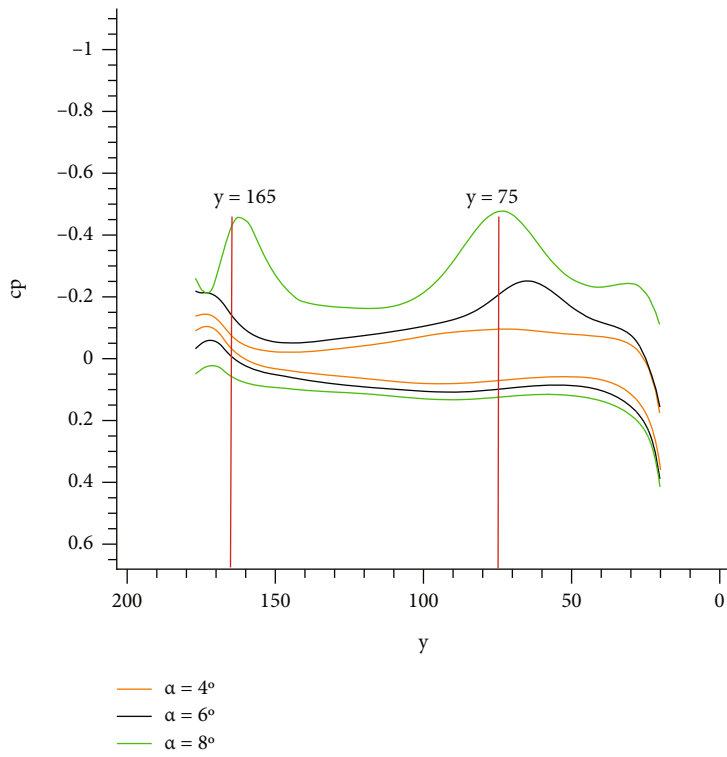
(b) Pressure distribution of the rear wing at 1/4 chord

FIGURE 21: Wingspan pressure distribution of the 60° model at $M = 0.75$ and $\alpha = 4°/6°/8°$.

which may cause some stability problems at $\alpha = 4°$ and $6°$ and $M = 0.75$. For the lift, the interference received by the rear wing is decreased with the increase in M and α. The upstream wake may reduce the airflow separation of the rear wing and improve the aerodynamic performance of the rear wing. Miura [41] referred that the rear wing of the low-speed and long-endurance UAV has less aerodynamically inter-

fered at low speeds. This result is quite different from the aircraft in this paper.

Figure 19 shows the drag characteristic of the 60° model at different Mach numbers. The drag difference between the front and rear wings is lower than that of the 15° model. The difference in the wing drag coefficient between $M = 0.75$ and $M = 0.9$ is slight. On the whole, compared with the 15°

model, the drag difference between the front wing and the rear wing decreases with the increase in M. At $M = 1.5$, the drag ratio between the front wing and the rear wing changes slightly with increasing α, and the extreme point is different from those at other Mach number states. On the whole, the retarding effect of the rear wing and telescopic rod on the front wing is reduced with the increase in the distance between the front wing and rear wing, and the drag characteristics of the front wing are improved.

Figure 20 shows the surface streamline pattern, the volume streamlines, and the c_p_distribution at wings for the 60° model. At $M = 0.75$, the front wing has a stronger spanwise flow than the rear wing, so the drag coefficient of the front wing increases faster than that of the rear wing after 4°. Moreover, as α increases, the spanwise flow on the wing's upper surface strengthens. Leading-edge vortex is generated at the leading edge of the front wing root, which has a beneficial effect on the wing, i.e., increasing the suction on the front wing's upper surface at $y = 70$ (Figure 21(a)). These phenomena increase the slope of the lift coefficient of the front wing in a transonic state.

However, at this angle of attack state with a supersonic freestream, the front wing does not have a leading-edge vortex lift, and separation occurs in the outer wing section, resulting in a decline of pressure and in a slight decrease in the slope of the lift coefficient (Figure 21(a)). As α increases, the airflow goes through the upper surface of the front wing, and the wing bracket to the rear wing with the spanwise flow at the rear wing strengthened gradually. Further, as α increases, the flow separation at the trailing edge of the front wing is enhanced in the spanwise direction when $M = 1.5$, resulting in a decrease in the slope of the front wing lift coefficient. For the rear wing, when $M = 0.75$ and $\alpha = 8°$, affected by the wake of the connecting bracket and the outer edge of the task module, the leading vortex of the wingtips and inner section of the rear wing increase the suction of the upper surface (Figure 21(b)), which is beneficial to the lift characteristics of the rear wing. For the supersonic state, the upper surface of the wing has a strong spanwise flow. The increase in α decreases the interference of upstream components, bringing about 120% extra suction to the upper surface of the rear wing at $y = 175$ (Figure 7(b)).

5. Conclusion

This study investigates the aerodynamic characteristics of a new-concept morphing aircraft at different flight conditions. According to the analysis results, the following conclusions are mainly obtained:

(1) The objective of this paper is a new-concept aircraft, which provides a new direction of morphing configuration. Moreover, a new form of morphing was designed: a variable swept wing with the diamond joined-wing configuration and a new large-scale variant actuation mechanism based on the "rack-type sliding rail" structure. The feasibility of the design is proven by the results of aerodynamic characteristics and flow field state at different Mach numbers. The morphing joined-wing aircraft can improve the aerodynamic characteristics at different Mach numbers by adjusting the sweep angle. As the sweep angle changes, the wing airfoil and the relative distance between the front and rear wings change significantly. Still, overall, a larger maximum lift-to-drag ratio can be obtained at different Mach numbers. The maximum lift-to-drag ratio is about 13.5 at $M = 0.5$, $\alpha = 4°$, and $\Lambda = 15°$, 12.8 at $M = 0.75$, $\alpha = 4°$, and $\Lambda = 15°$, and 3.4 at $M = 1.5$, $\alpha = 6°$, and $\Lambda = 15°$

(2) The advantages and disadvantages of this configuration are compared with the application of the morphing design in traditional tubby fuselage configuration and BWB configuration. The subsonic aerodynamic efficiency of the object of study is lower than that of the Firebee, but it has a better transonic aerodynamic characteristic, which expands to the supersonic state. Compared with the variable-sweep BWB configuration, the diamond joined-wing aircraft has better lift characteristics at subsonic and transonic states at $\alpha = 4°$, but there is a greater drag. This configuration and variable forward-swept wing configuration have similar maximum lift to drag ratios at different speed domains, but this configuration has lower zero-lift drag at supersonic speed, which means better supersonic sprint performance

(3) Numerical simulation is used to reveal the aerodynamic characteristics and interference characteristics of front and rear wings at different sweep angles and Mach numbers. Changing the wing spacing has a dual effect on the diamond joined-wing configuration. On the one hand, reducing the wing spacing can improve the lift performance of the aircraft. On the other hand, the reduction of the wing spacing will increase the interaction of the front wing and the rear wing and thus increase the drag of the rear wing. Meanwhile, changing the wing spacing can improve the separation characteristics of the front wing

(4) Compared with the conventional configuration of the diamond joined-wing, the front wing and the rear wing of the current aircraft are connected by the bracket, which acts like a winglet, so there is still a good pressure difference at the wingtip. However, the rear wing of this configuration will be interfered by the upstream components, which have a greater impact on the aerodynamics of the rear wing. As the angle of attack increases, the interference received by the rear wing becomes small, leading to the increase in the aerodynamic contribution of the rear wing to the aircraft. Meanwhile, as M increases, the interference received by the rear wing also becomes small at the same angle of attack. The interference characteristics are different between different sweep angles:

(i) For the 15° model, the inner wing section of the rear wing is far away from the upstream components, and the wake of the task module has increased the suction of the upper surface of the rear wing; the outer wing section of the rear wing is greatly interfered by the downwash of the front wing and the telescopic rod, which has an adverse effect on the lift of this section

(ii) For the 60° model, at the transonic state, under the action of the connecting bracket and the upstream wake, two leading-edge vortices appear on the upper surface of the rear wing at $Y = 75$ and $Y = 165$, which have a beneficial effect on the lift characteristic of the rear wing, but at the supersonic state, the upper surface of the wing has a strong spanwise flow, which brings greater drag to the rear wing

Abbreviations

A_w: Wing area (m^2)
C_D: Drag force coefficient
C_L: Lift force coefficient
K: Lift-to-drag ratio
K_max: Maximum lift-to-drag ratio
Re: Reynolds number
Ler: Characteristic length
α: Angle of attack (°)
Λ: Sweep angle (°)
C_p: Pressure coefficient
c: Chord (mm)
M: Mach number
a: Speed of sound
ρ: Density
x: Axial position (mm)
y: Spanwise position (mm)
z: Normal position (mm).

Data Availability

Part or all of the data or models generated or used in the research process are proprietary or confidential and can only be provided on a limited basis. All the data used in this paper have been obtained by calculations and tests conducted by this institution. Without the permission of the institute, we have no right to release these data sets.

Conflicts of Interest

The authors declare that they have no conflicts of interest.

References

[1] P. Bai, "Development status of key technologies and expectation about smart morphing aircraft," *Acta Aerodynamica Sinica Journal*, vol. 37, no. 3, 2019.

[2] R. Wlezien, G. Horner, A. McGowan et al., "The aircraft morphing program," in *39th AIAA/ASME/ASCE/ AHS/ASC Structures, Structural Dynamics, and Materials Conference and Exhibit*, Long Beach,CA,U.S.A, 1998.

[3] R. Ajaj, M. Friswell, E. S. Flores, O. Little, and A. Isikveren, "Span morphing: a conceptual design study," in *53rd AIAA/ASME/ASCE/AHS/ASC Structures, Structural Dynamics and Materials Conference*, Honolulu, Hawaii, 2012.

[4] T. Ivanco, R. Scott, M. Love, S. Zink, and T. Weisshaar, "Validation of the Lockheed Martin morphing concept with wind tunnel testing," in *48th AIAA/ASME/ASCE/AHS/ASC Structures, Structural Dynamics, and Materials Conference*, Honolulu, Hawaii, 2007.

[5] S. Barbarino, O. Bilgen, R. M. Ajaj, M. I. Friswell, and D. J. Inman, "A review of morphing aircraft," *Journal of Intelligent Material Systems and Structures*, vol. 22, no. 9, pp. 823–877, 2011.

[6] R. Pecora, A. Francesco, A. Gianluca, and C. Antonio, "Validation of a smart structural concept for wing-flap camber morphing," *Smart Structures and Systems*, vol. 14, no. 4, pp. 659–678, 2014.

[7] A. Maurizio, A. Francesco, and P. Rosario, "Numerical and experimental validation of a full scale servo-actuated morphing aileron model," *Smart Materials and Structures*, vol. 27, article 105034, 2018.

[8] G. Amendola, I. Dimino, M. Magnifico, and R. Pecora, "Distributed actuation concepts for a morphing aileron device," *The Aeronautical Journal*, vol. 120, no. 1231, pp. 1365–1385, 2016.

[9] A. Terrence, "Morphing aircraft systems: historical perspectives and future challenges," *Journal of Aircraft*, vol. 50, no. 2, pp. 337–353, 2013.

[10] J. Lv, "Rules of the optimal variable sweep wing in low and medium height," *Flight Dynamic*, vol. 34, 2016.

[11] J. Lv, C. Dong, and Y. K. Chen, "The analysis of the rule about variable sweep wing-body," *Nanchang Hangkong University*, 2016.

[12] A. Tarabi, S. Ghasemloo, and M. Mani, "Aerodynamic and performance evaluation of a variable-sweep morphing wing," *Transactions on Mechanical Engineering*, vol. 23, no. 6, pp. 2694–2703, 2016.

[13] S. Xinbing, J. Wen, and Z. Xiwei, "Study on the influence of swept angle on the aerodynamic characteristics of the cross-section airfoil of a variable swept-wing aircraft," *IOP Conference Series: Materials Science and Engineering*, vol. 685, no. 1, 2019.

[14] X. Li, F. Qian, and C. P. Li, "Design of morphing aircraft with variable-forward-swept wing under wild flight velocities," in *8th CSAA Science and Technology Youth Forum*, pp. 577–585, Jiangmen City, Guangdong Province, China, 2018.

[15] W. Liu, F. Wang, and X. Liu, "Aerodynamic characteristics and flow mechanism of the configuration with variable forward-swept wing," *Acta Aeridynamica Sinica*, vol. 28, no. 5, 2010.

[16] W. Liu, "Longitudinal characteristics of the aerodynamic configuration with variable forward-swept wing," *Flight Dynamic*, vol. 26, 2008.

[17] A. Brett and L. S. Robert, "Classical flight dynamics of a variable forward-sweep-wing aircraft," *Journal of Guidance*, vol. 9, no. 2, pp. 352–356, 1986.

[18] J. Wolkovitch, "The joined wing: an overview," *Journal of Aircraft*, vol. 23, no. 3, pp. 161–178, 1986.

[19] M. Samuels, "Structural weight comparison of a joined wing and a conventional wing," *Journal of Aircraft*, vol. 19, no. 6, pp. 485–491, 1982.

[20] I. Kroo, J. W. Gallman, and S. Smith, "Aerodynamic and structural studies of joined-wing aircraft," *Journal of Aircraft*, vol. 28, no. 1, pp. 74–81, 1991.

[21] E. Levine, "Aerodynamic of joined-wing airplane configurations: park work and future challenges-a survey," in *19th AIAA Applied Aerodynamics Conference*, pp. 16–19, Anaheim, CA, U.S.A, 1986.

[22] J. Pan, "An approach to possibility of direct force control on the joined wing configuration," *Flight Dynamics*, vol. 14, no. 1, 1996.

[23] G. Li, "The aerodynamics investigation of the joined-wing configuration," *Acta Aerodynamica Sinica Journal*, vol. 24, no. 4, pp. 513–518, 2006.

[24] J. Richards, A. Suleman, and T. Aarons, "Multidisciplinary design for flight test of a scaled joined wing sensor craft," in *AIAA/ISSMO Multidisciplinary Analysis Optimization Conference*, Fort Worth, Texas, 2010.

[25] H. Djojodihardjo, "Conceptual design and aerodynamic study of joined-wing business jet aircraft," in *28TH International Congress of the Aeronautical Sciences*, Brisbane, Australia, 2012.

[26] T. Chau and D. Zingg, "Aerodynamic design optimization of a transonic strut-braced-wing regional aircraft," *Journal of Aircraft*, vol. 59, no. 1, pp. 253–271, 2022.

[27] C. Rasmussen, "Joined-wing sensor-craft configuration design," *Journal of Aircraft*, vol. 43, no. 5, 2006.

[28] Y. Guo, "Research on aerodynamic characteristics of a box wing configuration," *Aeronautical Computing Technique*, vol. 42, no. 2, 2012.

[29] M. Skillen and W. Crossley, "Conceptual morphing aircraft sizing using a multi-level optimization strategy," in *46th AIAA Aerospace Sciences Meeting and Exhibit*, Reno, Nevada, 2008.

[30] M. Skillen and W. Crossley, "Developing morphing wing weight predictors with emphasis on the actuating mechanism," in *14th AIAA/ASME/AHS Adaptive Structures Conference*, AIAA Paper 2006-2042, 2006.

[31] S. Philippe and A. Steven, "A one-equation turbulence model for aerodynamic flows," in *30th Aerospace Sciences Meeting & ExhlbH, Paper 1992-439*, Reno,NV,U.S.A, 1992.

[32] K. Soshi and F. Kozo, "Time-series and time-averaged characteristics of subsonic to supersonic base flows," *AIAA Journal*, vol. 45, no. 1, pp. 289–301, 2007.

[33] E. Lynch and M. Smith, "Hybrid RANS-LES turbulence models on unstructured grids," in *38th AIAA Fluid Dynamics Conference and Exhibit, AIAA Paper 2008-3854*, Seattle, Washington, 2008.

[34] Y. Huang, J. Pei, P. V. Nielsen et al., "Chapter 4 - experimental techniques," in *Industrial Ventilation Design Guidebook (Second Edition)*, pp. 185–277, 2021.

[35] B. Yan, "Aerodynamic analysis, dynamic modeling, and control of a morphing aircraft," *Journal of Aerospace Engineering*, vol. 32, no. 5, 2019.

[36] J. Anderson, *Aircraft Performance and Design*, The McGraw-Hill Companies, Inc, Boston, 1999.

[37] Q. Chen, P. Bai, and F. Li, "Morphing aircraft wing variable-sweep: two practical methods and their aerodynamic characteristics," *Acta Aerodynamica Sinica*, vol. 30, no. 5, pp. 658–663, 2012.

[38] W. Liu and F. Wang, "A new aerodynamic configuration of UAV with variable forward-swept wing," *Acta Aerodynamic Et Astronautica Sinica*, vol. 30, no. 5, pp. 832–836, 2009.

[39] J. Sun, "Aerodynamic numerical analysis of the low Reynolds number diamond joined-wing configuration unmanned aerial vehicle," *International Journal of Aeronautical and Space Sciences*, vol. 19, no. 3, pp. 544–562, 2018.

[40] J. Anderson, *Fundamentals of Aerodynamics*, McGraw-Hill, New York, 4th ed. edition, 2010.

[41] H. Miura, A. Shyu, and J. Wolkovitch, "Parametric weight evaluation of joined wings by structural optimization," *Journal of Aircraft*, vol. 25, no. 12, pp. 1142–1149, 1988.